Geological history of the Atira Mons large shield volcano, Beta Regio, Venus.

C.H.G. Braga [a,b], E.G. Antropova [c], R.E. Ernst [b,*], H. El Bilali [b], J.W. Head [d], K.L. Buchan [e]

[a] *Department of Earth and Environmental Sciences, University of Ottawa, Ottawa, Canada*
[b] *Department of Earth Sciences, Carleton University, Ottawa, Canada*
[c] *Faculty of Geology and Geography, Tomsk State University, Tomsk, Russia*
[d] *Department of Earth, Environmental and Planetary Sciences, Brown University, Providence, RI, USA*
[e] *273 Fifth Ave, Ottawa, Canada*

A B S T R A C T

Atira Mons is a large (~300,000 km^2) low-relief (1.8 km) shield volcano, with individual flows extending up to ~700 km from the central caldera. It is located about 3000 km NW from the major plume center Beta Regio. Detailed mapping of the flows (at 1:500,000 scale, 10x more detailed than previous mapping) has identified fifty-three flow units which are grouped into eleven packages. Flow units are distinguished based on radar brightness, topography, morphology, continuity, structural modification, and sources, while flow packages group flows with clear stratigraphic relationship affinity.

Cross-cutting relationships indicate a complex and multi-episodic eruption history with provisional identification of six mapped stages. The most voluminous flows are concentrated in the early stages, while the younger pulses, with a few exceptions, are shorter and less voluminous. A central caldera hosts the youngest volcanism with flows breaching its eastern side. Multiple stages of caldera collapse are indicated.

The volume of the volcano is estimated using various methods and yields values range from ~47,000 to ~270,000 km^3. The larger estimates are consistent with that of the magma volume of Large Igneous Provinces (LIP) on Earth. An appropriate terrestrial analogue is the Benham Rise Oceanic LIP in the western margin of the Philippine Sea, and particularly the Apolaki Caldera, which is the world's largest known basaltic caldera with a diameter of ~150 km.

1. Introduction

1.1. Overview of Venus

Venus shares many important planetary parameters with Earth, including size, mass, position in the Solar System, presence of an atmosphere, but is radically different in terms of other parameters, such as the absence of an intrinsic magnetic field, a dense CO_2-rich atmosphere, lack of water on the surface, very high surface pressure (~93 bar) and temperature (~740 K) (Solomon et al., 1992; Basilevsky and Head, 2003; Barsukov et al., 1986; Barsukov, 1992). Venus also does not show signs that plate tectonics is currently active, evidenced by the lack of observable plate boundaries (Phillips and Hansen, 1994). However, some recent publications indicate that tesserae may preserve an earlier history that involved lateral accretion and potential plate tectonics (Way et al., 2016, 2022; Gilmore and Head, 2018; Khawja et al., 2020; Byrne et al., 2021). Magmatism on Venus is thought to be currently operating predominantly in a single-plate, stagnant-lid regime, with all magmatism occurring in intraplate settings (Head et al., 1992; Ernst and Desnoyers, 2004; Solomatov and Moresi, 1996; Stern et al., 2018), with the largest events being of similar scale (minimum volume 100,000 km^3) to Large Igneous Provinces (LIPs) on Earth (Head and Coffin, 1997; Buchan and Ernst, 2021; Ernst, 2014).

About 168 large shield volcanoes are recognized on Venus with diameters ranging from ~100 to ~1000 km (Crumpler and Aubele, 2000; Crumpler et al., 1997). The volcanic flow history of only a few Venusian Montes have been mapped in any detail (e.g., Maat Mons by Mouginis-Mark, 2016), at an estimated scale of 1:2,500,000, although more detailed mapping at a scale of 1:500,000 is in progress for Maat Mons (El Bilali et al., 2022), and Tullikki Mons (Ivanov et al., 2019). Detailed mapping of individual Montes is necessary to better understand their emplacement histories and for comparison with large shield volcanoes on Earth. Herein we provide detailed geological mapping of Atira Mons.

1.2. Selection of Atira Mons for detailed mapping and objectives

Understanding the history of volcanism and individual volcanoes is of utmost importance in unravelling the geologic evolution of Venus and the role of volcanic processes in shaping the surface. This work examines the stratigraphy and evolution of the large shield volcano Atira Mons

---

Fig. 1. Oblique view of Atira Mons (green line) as seen in SpaceEngine. Estimated area ~300,000 km^2 (https://spaceengine.org/).

(Fig. 1) in the NW portion of the plume center Beta Regio (Basilevsky and Head, 2007, Fig. 2), probably superimposed on the volcanic plains Kawelu and Guinevere Planitiae.

The main goal of this work is to reconstruct the exposed geologic history of the large shield volcano Atira Mons, and gain insights on the relative timing and scale of its different evolutionary stages and its impacts on the evolution of the Venusian surface.

The main objectives of this work are:

- Provide a detailed geologic map on a scale of 1:500,000 and a stratigraphic column for Atira Mons.
- Identify, map, and characterize all visible geologic units related to or located in the vicinity of Atira Mons.
- Identify/infer and characterize the type of source for each lava flow unit (magma reservoir, fissures, vents, small shield volcanoes, etc.).
- Develop a detailed history of the exposed flow units of the volcano, considering the relationship between their source locations and the relative timing of eruptions.
- Recognize and outline the limitations of the current datasets.

The novelty of this work lies in the detailed mapping on a 1:500,000 scale, since Atira Mons has previously not been mapped beyond the 1:5,000,000 scale (Dohm et al., 2011). Using a similar approach to MacLellan et al. (2021), we aimed to achieve new insights and

discoveries regarding the history and evolution of this major volcanic center. We also refine the methodology for mapping at such detail, which will be applicable to future mapping of other major volcanic features on the Venusian surface.

1.3. Previous research on Atira Mons' study area

There are a handful of previous studies related specifically to Atira Mons. Its gravity anomaly was modeled by Kiefer and Potter (2000) to estimate elastic lithospheric thickness. The authors only estimated an upper boundary for this parameter at 10 km, since field resolution of the gravity dataset is smaller at high latitudes. Herrick et al. (2005) noted that Atira Mons has a low-magnitude negative isostatic anomaly. Later, using the gravity and altimetry datasets of the Magellan mission, Jiménez-Diaz et al. (2015) modeled the average crustal thickness for Venus to be usually 20–25 km, and in the vicinity of Atira Mons approximately 15–20 km. Based on this global model, they calculated the effective elastic thickness in the area of Atira Mons to be 25–40 km.

Basilevsky and Head (2000) compiled a global map of rift systems and large volcanoes. They described Atira Mons as a "transitional" volcano (of relative age between "old" and "young") composed of flows both superposed on the regional plains and contemporaneous with the plains, i.e., they overlap in age with wrinkle-ridged plains units. Ernst et al. (2003) described graben-fissure systems (interpreted to overlie mafic dyke swarms) in Guinevere Planitia and Beta Regio, which includes Atira Mons. Here, using geologic mapping from Basilevsky et al. (1999) and Basilevsky and Head (2000). Ernst et al. (2003) interpreted that part of the volcanism of Atira Mons, a lobate plains unit (Pl), postdates the formation of its main radiating graben-fissure system, R2 (Fig. 3a), as well as most of the other regional graben-fissure systems, except for the circumferential system, C3 (Fig. 3a). Atira Mons was further described in the Geologic Map of the Metis Mons Quadrangle (V-6) mapped on a scale of 1:5,000,000 (Dohm et al., 2011) (Fig. 3b). Here, the authors divided the volcano into an upper and a lower unit (Fig. 3b). Older Atira Mons material (mA$_1$) is interpreted to consist of rough to smooth lava flows sourced from the summit caldera. This unit represents primary phases of volcanic activity at Atira Mons. Younger Atira Mons material (mA$_2$) is interpreted to consist of smooth lava flows sourced from small volcanoes during and after emptying of an underlying magma chamber.

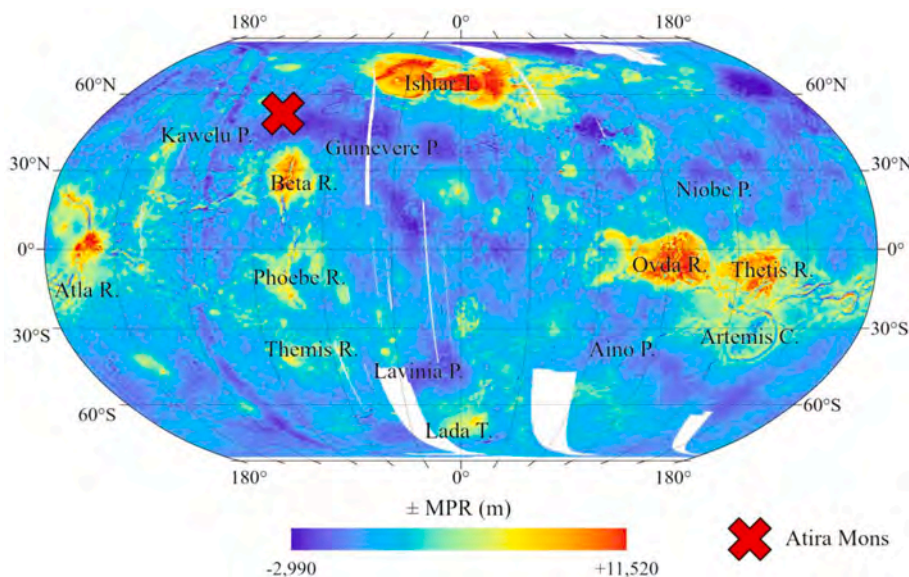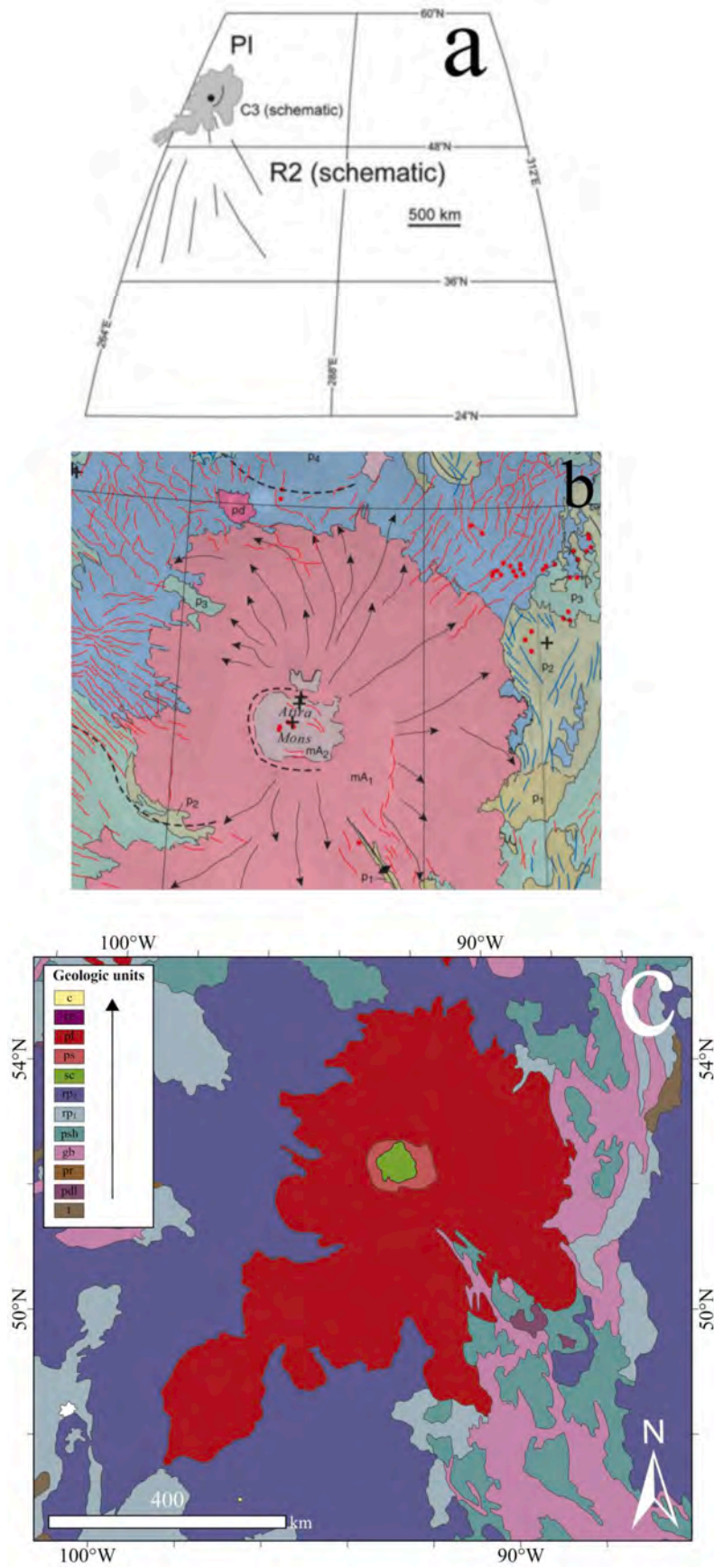Atira Mons was shown by Ivanov and Head (2011) as part of their

Fig. 2. Global Venus Magellan altimetry (Robinson Projection) showing major geographic features and the location of Atira Mons. P – Planitia; R. – Regio; T – Terra; C – Corona; ±MPR (m) – meters above or below mean planetary radius.

(caption on next page)

Fig. 3. Previous geological maps of the study area. a) Relationship between radiating (R2) and circumferential (C3) graben–fissure systems (interpreted to overlie dykes) (after Ernst et al., 2003) and geologic unit Pl (lobate plains unit) (after Basilevsky et al., 1999) at Atira Mons; b) Fragment extracted from Geologic Map of the Metis Mons Quadrangle (V-6) (Dohm et al., 2011), where mA_1 and mA_2 represent Older and Younger Atira Mons material, respectively. Arrows point in interpreted flow direction. c) Fragment extracted from global map of Ivanov and Head (2011) (c – impact craters; rz – rift zones; pl – lobate plains; ps – smooth plains; sc – shield cluster; rp_2 – upper regional plains; rp_1 – lower regional plains; psh – plains with shield volcanoes; gb – groove belts; pr – ridge plains; pdl – densely lineated plains; t – tesserae). Arrow points in younging direction.

global geologic map of Venus (Fig. 3c) on a scale of 1:10,000,000. Here the volcano's flanks are composed of lobate plains (pl), while its summit is made up of a cluster of shield volcanoes (sc) and smooth plains (ps). Generally, Atira Mons partly covers the upper and lower units of regional plains (rp_{1-2}), plains with shield volcanoes (psh) and groove belts (gb).

2. Methodology

2.1. Data and software

Geologic mapping was carried out using full-resolution (75 m/pixel) Left-Look SAR (synthetic aperture radar) images and altimetry data (10–30 km diameter footprint; 80–100 m vertical resolution) from NASA's Magellan mission (1989–1994) (Ford et al., 1993) in ArcGIS Pro (https://esri.com/en-us/arcgis/products/argis-pro/overview). To enable more accurate and detailed interpretations, ArcGIS Pro and Java Mission-Planning and Analysis for Remote Sensing (JMARS) (Christensen et al., 2009) were used for regional reconnaissance and to create topographic profiles. Additionally, ArcGIS Pro and SpaceEngine (https://spaceengine.org/) were used to supply oblique views of the study area. ArcGIS Pro was further used to estimate the minimum volume of the volcano (details in Appendix A).

2.2. Approach to mapping

The geologic mapping carried out in Atira Mons at a scale of 1:500,000 follows the principles described in Tanaka (1994) and Wilhelms (1990). A geologic (or stratigraphic) unit is defined as rock bodies that formed simultaneously due to a specific process or a set of processes during a given time interval. In the context of mapping Venus' surface and Atira Mons, the main aspects considered to define a geologic unit are radar brightness, topography, morphology, and continuity. Basic stratigraphic principles, such as the principle of superposition and cross-cutting and embayment relationships form the basis on which stratigraphic columns were compiled. Where structural modification is pervasive and hampers the identification of the underlying geology, separate structural-material units were defined (see "Discussion" in Ivanov and Head, 2011).

Geologic units were gathered into distinct groups if their age relationships were confirmed by our criteria (see "2.3" below). Relative ages between separate groups were established by using marker units that show evidence for cross-cutting and embayment relationships.

2.3. Criteria for age relationships

The criteria used to determine the relative ages of geologic units were:

- Linear features (grabens, fractures, wrinkle ridges, and other lineaments) that cut across lava flows are younger than the flows.
- Cross-cutting or embaying flows are younger than the flows they cut or embay.
- The better preserved are the lobes of a given flow, the more likely it is that it is a younger unit.
- Flow units defined as a single polygon originating from a clear source region are usually the youngest units in a given area.

- Lava flows that show continuity along their length, but gradually change radar brightness, are considered part of the same unit, based on the fact that along-flow changes in lava rheology are known to occur on terrestrial lavas (e.g., Walker, 1973; Pinkerton and Norton, 1995; Griffiths, 2000), and are predicted for lava flows on Venus (e. g., Head and Wilson, 1986; Wilson and Head, 1983).

3. Results

3.1. Morphology and regional setting

Atira Mons is a large shield volcano with slopes varying from $\sim 0°$ to $\sim 7.5°$; average slope $\sim 0.26°$ (calculated using the "Add Surface Information" from the ArcGIS Pro tool, 3D Analyst) (Fig. 4). Like other large shield volcanoes on Venus (Stofan et al., 2001), Atira Mons is divided into an edifice that includes the summit and flanks with steeper slopes, and an outer flow apron, where slopes are shallower (Fig. 4c). It is centered at 51.4°N, 272.9°E (92.9°W) ~ 3000 km NW of Beta Regio, a major mantle plume center (Basilevsky and Head, 2007; Shimolina et al., 2023), and covers an area of $\sim 300,000$ km^2, with a width of ~ 681.7 km, a length of ~ 1035.2 km (longest dimension is to the SW) and a height of ~ 1.8 km. In our case, height was determined as the difference between the lowest (-200 m) and highest ($+1600$ m) elevations above or below the mean planetary radius (MPR) inside the volcano's perimeter. Although no direct geochemical data is available for Atira Mons, its shallow slopes, and the morphology and length of its lava flows are consistent with basaltic lavas (Grimm and Hess, 1997). Such generalization is further supported by the geochemical data of the Venera and VeGa landers (Kargel et al., 1993), which detected mafic compositions on all seven landing sites. Therefore, we interpret Atira Mons as basaltic volcano capped by a multiple-event, resurgent, asymmetric and elliptical caldera (recommendations for caldera descriptions summarized in Cole et al., 2005 and references therein), which ranges from ~ 115.8 to ~ 138.5 km in diameter (using minimum bounding geometry with a convex hull from 3D Analyst) (https://www.esri.com/en-us/arcgis/products/arcgis-3d-analyst/overview). In the global context, the volcano is located between Kawelu and Guinevere Planitiae, being the youngest major global geologic unit, superposed on groove belts (gb), Kawelu and Guinevere Planitiae (regional plains: rp_{1-2}), and plains with shield volcanoes (psh) (Ivanov and Head, 2011).

A field of small shield volcanoes (Fig. 4, sh) is located immediately NE of the Atira Mons' flows. These small volcanoes and their associated flows appear to be younger than the regional plains but have an uncertain age relationship with respect to Atira Mons. On the south flank, the volcano's flows partially cover a cluster of coronae and corona-like features (Fig. 4, ccl), including Davies Patera, and are covered by a dark craterless blast halo (Fig. 4, cbh) (cf. Antropova et al., 2023; Crumpler and Aubele, 2000).

The regional topography (Figs. 4b and 5) of Atira Mons and adjacent areas shows that lava flows extend radially downslope away from the summit region until they reach a topographic barrier (elevated terranes) on the west-southwestern ridge (rdg, Fig. 4) and eastern terminations (gb, Fig. 4) of the volcano. The W-, NW- and N-trending flows start radially from outside the caldera rim, but eventually swing 40-50° towards a local sub-circular depression (basin) of unknown origin ~ 300 km NW of the summit (db, Fig. 4). On Kawelu Planitia (kp, Fig. 4), where topography is more subdued, flows can be traced ~ 700 km to the SW away from Atira Mons' summit. Additionally, a change in flow width is
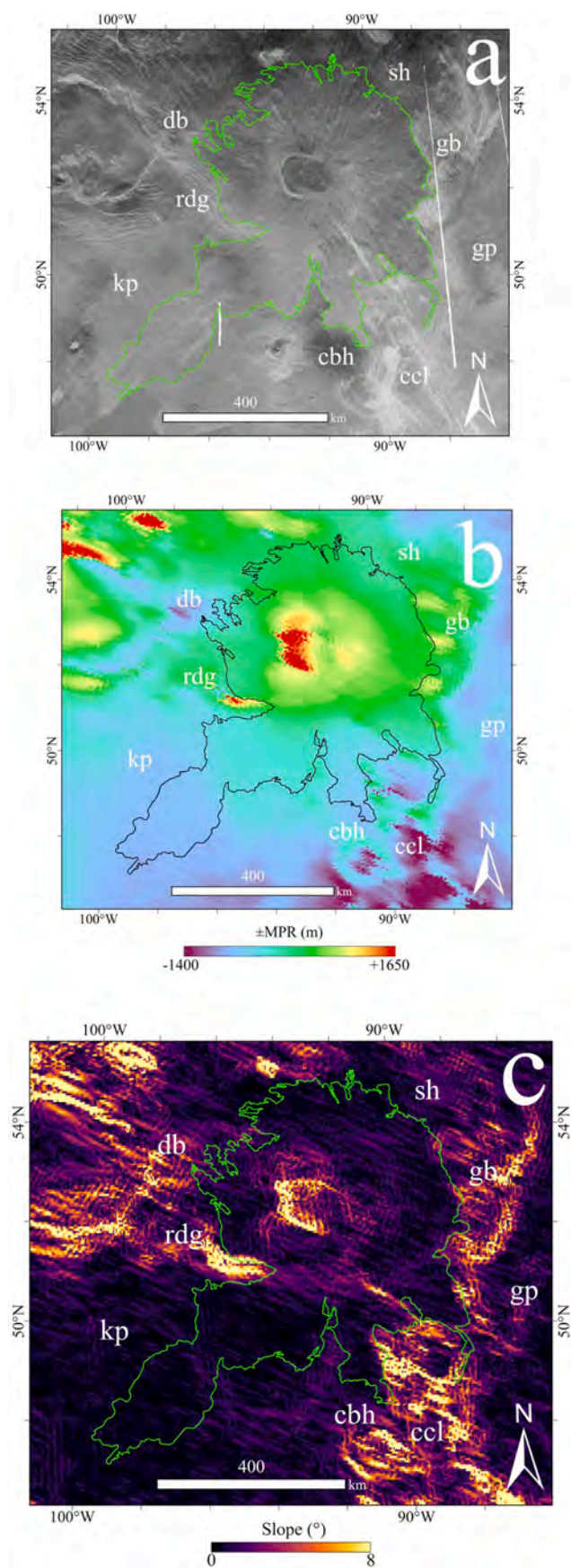
Fig. 4. Atira Mons' (green line) Magellan's SAR images and altimetry. a) Atira Mons (green line) on Magellan's left-look SAR images; gb (groove belts) after Ivanov and Head, 2011; sh – plains with shield volcanoes; ccl – corona cluster (including Davies Patera); cbh – craterless blast halo; kp – Kawelu Planitia; gp – Guinevere Planitia; db – deformed basin; rdg – west-southwestern ridge; b) Atira Mons (black line) on Magellan's altimetry; ±MPR (m) – meters above or below mean planetary radius. Other acronyms are the same as in part "a" c) Slope map of Atira Mons (green line). Other acronyms are the same as in part "a".

correlated with the influence of preexisting topographic barriers (e.g. rdg, Fig. 4) and slight changes in slope downhill (e. g., flow package SWb, see Fig. 4c and SW-NE profile in Fig. 5 between markers 15–17), with steeper slopes associated with narrowing of flows, while shallower slopes favor widening of flows. This is the expected behavior for Newtonian fluids (Figs.. 4c and 5, Profile SW-NE, marker 16; Gregg and Fink, 2000; Wadge and Lopes, 1991), indicating that at least part of the current regional topography already existed before these flows were emplaced.

3.2. Geological map of Atira Mons

A miniature of Atira Mons' 1:500,000 scale map is displayed in Fig. 6. Mapping resulted in the identification of sixty geologic units, consisting of fifty-three volcanic units (f – flows, sh – shield volcanoes), one gradational unit (g), one structural-material unit (rdg) and five units of uncertain origin (u). Additionally, three types of structures (s) were identified: arcuate fractures (sAF-1, sAF-2), wrinkle ridges (sWR) and polygonal fractures (sPF). Eleven flow packages are displayed in Fig. 7, while the location and density of forty-eight confirmed or inferred flow sources are shown in Fig. 8.

Below is a description of each of the map units. Table B1 (Appendix B) contains information on the exposed area, source number, present source elevation, maximum slope, mean radar backscatter and maximum flow length of each unit (when applicable). Additionally, Table B2 (Appendix B) contains information on the number, group, coordinates (latitude and longitude, decimal degrees), location (summit or flank) and type (confirmed/assumed vent or fissure) of each source.

3.3. Summit units (Smt)

Geologic units belonging to the summit units (Smt) are displayed in Fig. 9, while a general location of the area is displayed on Fig. 7:

fSmt-1: the lava flows of this unit comprise the C-shaped rim of Atira Mons' summit and are exposed over an area of ~1900 km^2. This unit is characterized by high radar brightness and the highest slopes of Atira Mons (~7.5º; Fig. 4c). It is partially covered by fSmt-2, fSWc-8, gSmt-1 and fNb-5, and its lower stratigraphic boundary is poorly constrained. The shape of the rim can be associated with caldera collapse processes, lava ponding, or related to younger flows covering its eastern portion (see Section 5.2). Sources for this unit are unclear and are assumed to be buried vents on the summit.

gSmt-1: the only gradational unit related to Atira Mons is interpreted to represent radar-bright landslides that originated from the caldera rim (fSmt-1). These are distinguished from flow units (f) by lacking the characteristic lobate morphology, having a brighter radar signature than the underlying flank flows and being spatially associated with the steeper slopes of Atira Mons' rim (up to ~7.5º; Fig. 4c). They occupy an area of ~700 km^2 that is restricted to the NW portion of Atira Mons' summit. These landslides crosscut fSWc-8 and fNa-7 and are partially covered by fSmt-2 and fNa-9.

fSmt-2: these flows are exposed over an area of ~3200 km^2 on the western portion of Atira Mons' summit. They are composed of radar-intermediate to radar-dark lavas that are deformed by polygonal fractures (sPF) and a small set of arcuate fractures (sAF-1). As with fSmt-1, the sources of these flows are obscured and assumed to be buried vents
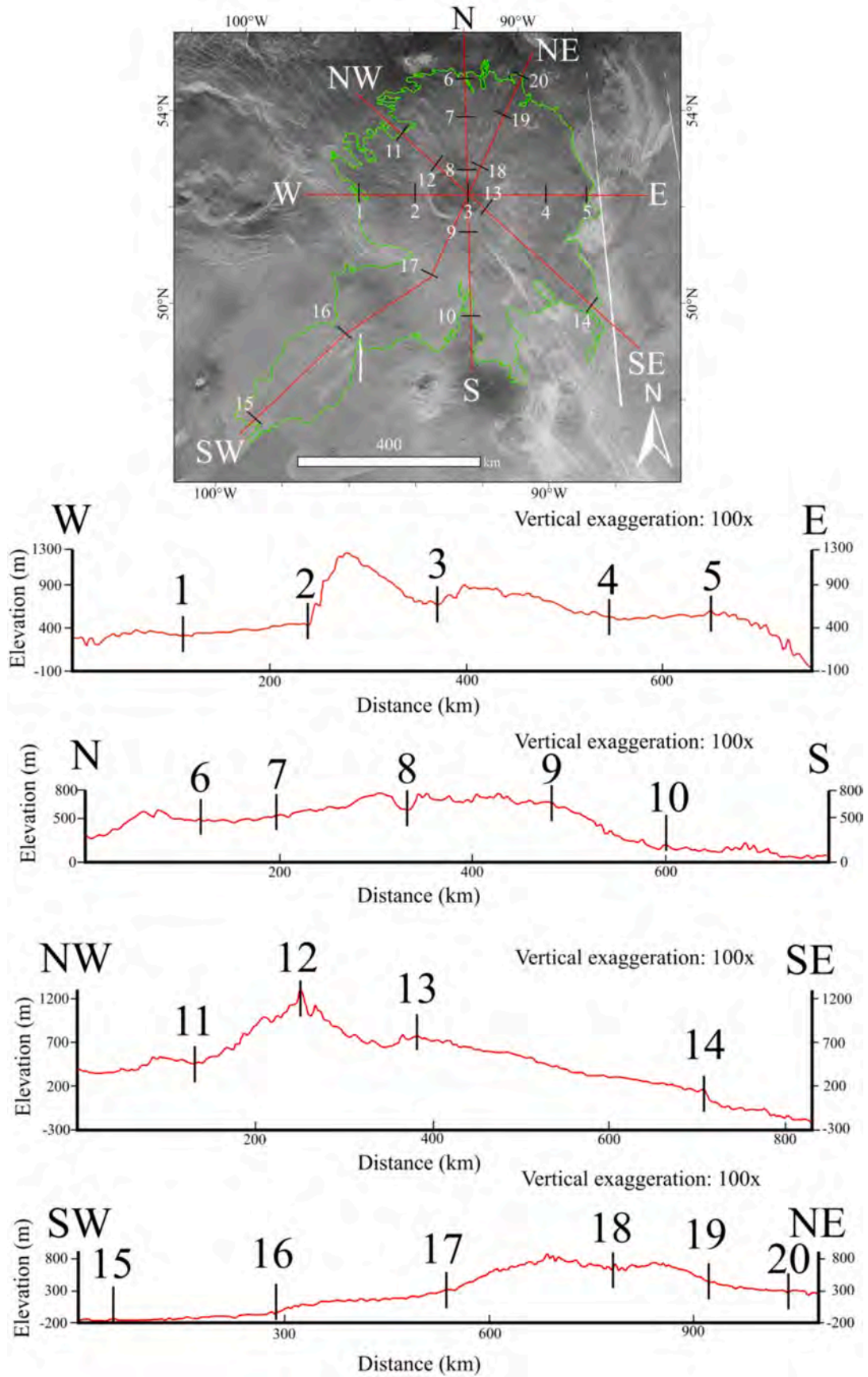
Fig. 5. Topographic profiles (red lines) of Atira Mons. Numbered ticks on profiles correspond to markers on the SAR image.

LEGEND

Summit units (Smt)

Volcanics
- shSmt-1
- fSmt-3
- fSmt-2
- fSmt-1

Gradational
- gSmt-1

Southwestern units (SW)

Volcanics
- fSWa-3
- fSWa-2
- fSWa-1
- fSWb-5
- fSWb-4
- fSWb-3
- fSWb-2
- fSWb-1
- fSWc-8
- fSWc-7
- fSWc-6
- fSWc-5
- fSWc-4
- fSWc-3
- fSWc-2
- fSWc-1

Northern units (N)

Volcanics
- fNa-9
- fNa-8
- fNa-7
- fNa-6
- fNa-5
- fNa-4
- fNa-3
- fNa-2
- fNa-1
- fNb-6
- fNb-5
- fNb-4
- fNb-3
- fNb-2
- fNb-1

Eastern units (E)

Volcanics
- fEa-2
- fEa-1
- fEb-5
- fEb-4
- fEb-3
- fEb-2
- fEb-1
- fEc-6
- fEc-5
- fEc-4
- fEc-3
- fEc-2
- fEc-1
- fEd-3
- fEd-2
- fEd-1

Western units (W)

Volcanics
- fW-1

Structural units (s)
- sAF-1
- sAF-2
- sPF
- sWR

Other units
- uSmt-1
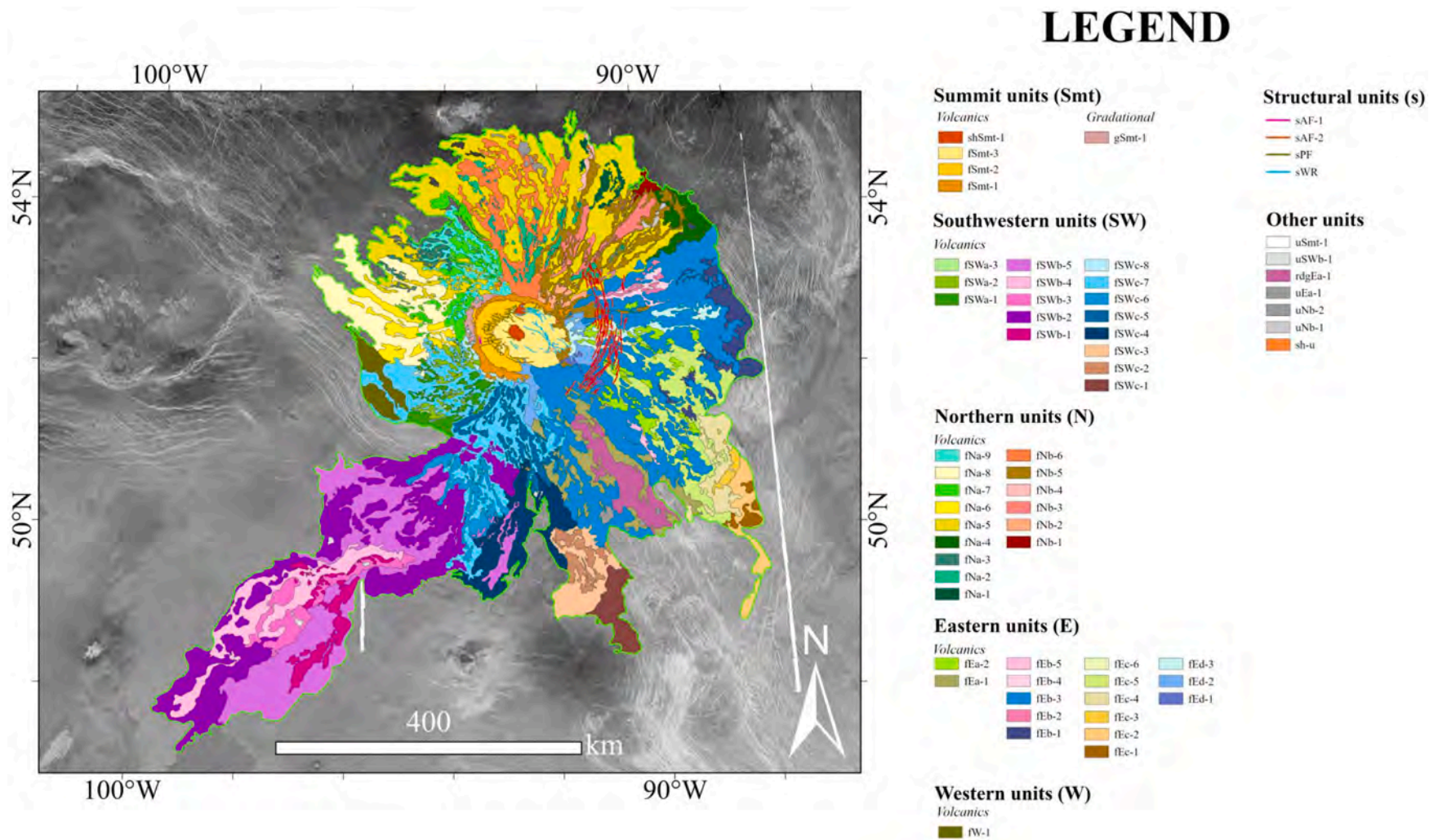- uSWb-1
- rdgEa-1
- uEa-1
- uNb-2
- uNb-1
- sh-u

Fig. 6. Geologic map of Atira Mons. f – lava flows (flucti); sh – shield volcanoes; s – structural units; g – gradational units; structural-material units (rdg); u – units of uncertain origin.
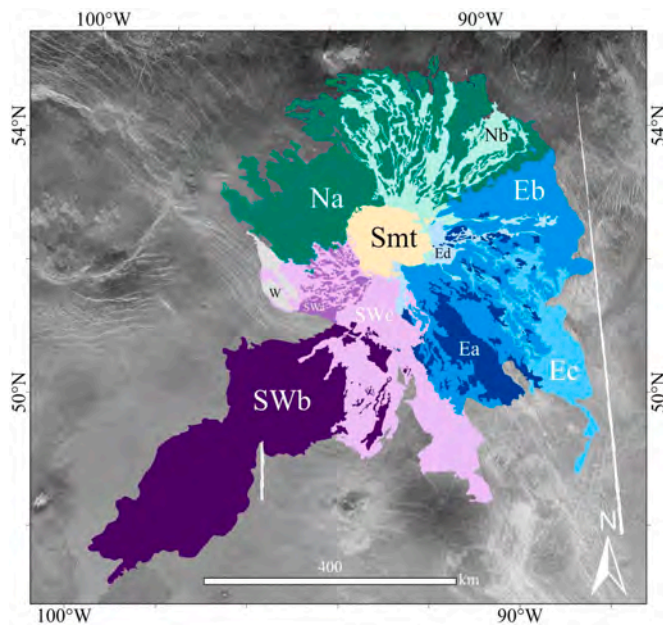
Fig. 7. Flow package map of Atira Mons. Colors assigned to them are for illustration purposes, and do not indicate relative ages. Smt – Summit units; SWa, SWb and SWc – Southwestern units "a", "b" and "c"; Na, Nb – Northern units "a" and "b"; Ea, Eb, Ec and Ed – Eastern units "a", "b", "c" and "d".

on the summit. Stratigraphically, these flows partially cover fSmt-1 and gSmt-1 and are partially overlain by radar-dark flows of fSmt-3.

fSmt-3: radar-dark flows that dominate the summit region, occupying an area of ~4900 km^2. These lavas partially cover fSmt-2 and fNb-5, and fill sPF. These flows are interpreted to be sourced from the vents and shield volcanoes (shSmt-1) of the summit region and are among the youngest units of Atira Mons. Topographic data show that some of the flows of this unit seem to be running uphill, suggesting that the last episode of caldera subsidence happened in the later stages of development of Atira Mons.

shSmt-1: shield volcanoes emplaced on the top of fSmt-2 and fSmt-3. Their diameter varies from ~13 to ~23 km, and they are thought to be the sources for flows fSmt-3. Overall, these volcanoes occupy an area of ~470 km^2 and are identified by their topographic signature on the left-looking SAR data, which shows their left side illuminated in comparison with their right side (Ford et al., 1993), and their similarities to other small shields on Venus (e.g., Ivanov and Head, 2004).

3.4. Southwestern units (SW)

The geological maps of the southwestern flow packages "a", "b", and "c" are displayed on Figs. 10–12, respectively with the general location shown in Fig. 7.

3.4.1. fSWa units

fSWa-1: radar-intermediate flow lobes probably sourced from flank vents at the boundary of the summit region. These flows have maximum length of ~100 km and their exposed area is equal to ~2800 km^2. They terminate at the topographic barrier marked by a set of arcuate fractures on Atira Mons' west-southwest (rdg, Fig. 4). Flows from fSWa-1 are crosscut by fSWc-8, fSWc-7, and fSWa-2, but have an ambiguous relationship with fNa-8.

fSWa-2: radar-bright flows originating from the same source as fSWa-1, i.e., flank vents located at the boundary of the summit region. These flows are exposed over an area of ~1600 km^2 and have maximum length of ~70 km. fSWa-2 crosscuts fSWa-1 and is crosscut by fSWa-3 and fSWc-8.

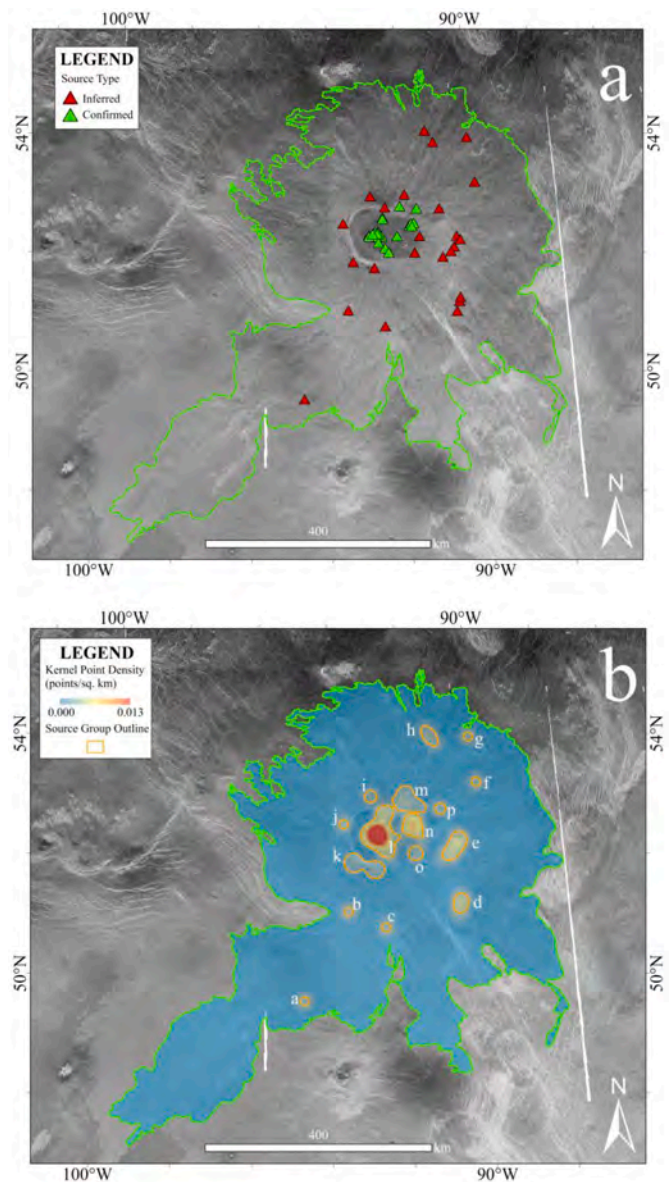fSWa-3: linear shaped radar-dark flow that crosscuts fSWa-1 and

Fig. 8. Maps of source locations and density of sources per square kilometer. a) Location of inferred and confirmed sources on Atira Mons. Green outline marks the perimeter of the volcano b) Map showing density of sources per square kilometer. Letters indicate source groups in Tables B1 and B2 (see Appendix B).

fSWa-2 and is crosscut by fSWc-7. It occupies an area of ~80 km^2, has a maximum length of ~35 km, and its source is unknown.

3.4.2. fSWb units

fSWb-1: flank-sourced, radar-bright lobate flow located ~300–350 km southwest of Atira Mons' summit. It occupies an area of ~3900 km^2, has a maximum length of ~230 km, and is crosscut by fSWb-2, fSWb-3, and fSWb-4.

fSWb-2: radar-intermediate flow that occupies an area of 28,800 km^2 and terminates ~700 km away from Atira Mons' summit. This is the longest flow associated with Atira Mons, having a visible length of ~580 km. Its radar brightness changes downslope, suggesting along-flow changes, something observed on Earth (e.g., Walker, 1973; Pinkerton and Norton, 1995; Griffiths, 2000) and not always on Venus (e.g., MacLellan et al., 2021; Mouginis-Mark, 2016). This unit crosscuts fSWb-1 and is crosscut by fSWb-3, fSWb-4, fSWb-5, fSWc-4, fSWc-6, and fSWc-7. A source is not visible but inferred. It could be on the flanks and coincide with the source for fSWc-6. Alternatively, the flow may have
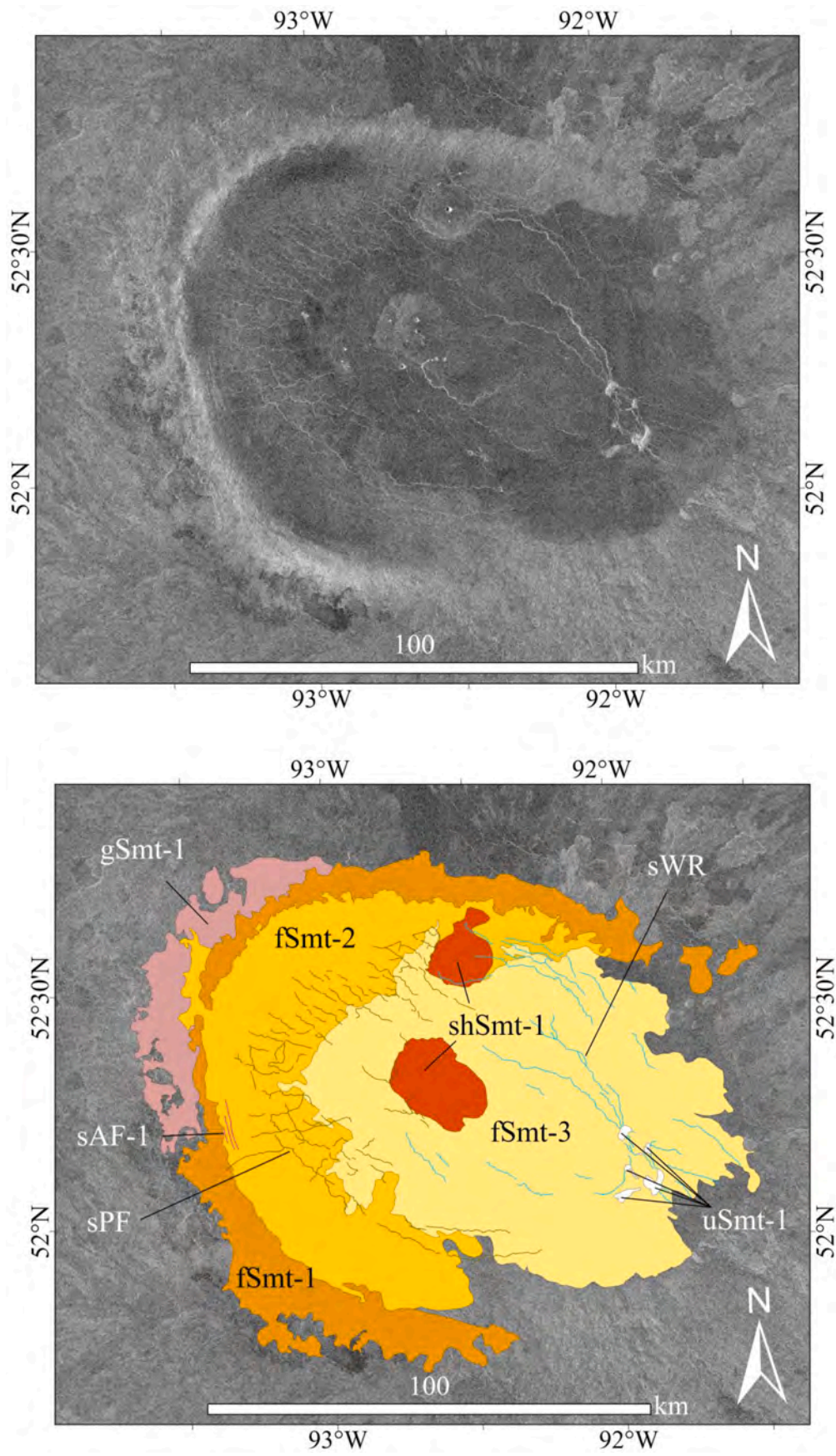
Fig. 9. SAR image (top) and geologic map (bottom) of the summit units. Geological units are described in the text and Table B1 (Appendix B).
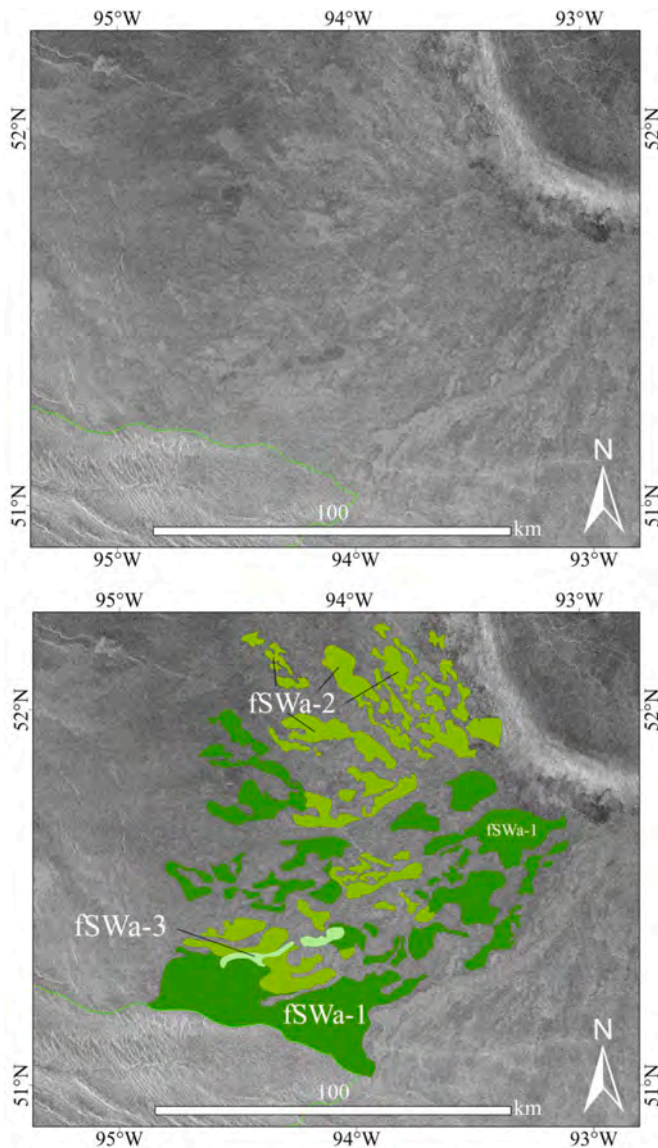
Fig. 10. SAR image (top) and geologic map (bottom) of the southwestern flow package "a". Green line marks Atira Mons' outer boundary. Geological units are described in the text and Table B1 (Appendix B).

originated at the summit or along its margin.

fSWb-3: radar-intermediate flow lobe sourced from the same flank-source as fSWb-1. It crosscuts fSWb-1 and fSWb-2 and is partially covered by fSWb-4 and fSWb-5. As with some other Venusian flows, these lavas show a brighter radar signature on their boundaries in comparison with their core (Byrnes and Crown, 2002). These flows occupy an area of ~4300 km^2 and have a maximum length of ~230 km.

fSWb-4: radar-intermediate to radar-dark flow lobes sourced from the same source as fSWb-1 and fSWb-3. They crosscut fSWb-1, fSWb-2, and fSWb-3. They occupy an area of ~8200 km^2 and have a maximum length of ~385 km^2.

fSWb-5: radar-intermediate to radar-dark flow lobes sourced from the same flank source as fSWb-2 and fSWc-6, or from the summit. Their length of ~510 km and exposed area of ~23,600 km^2 are comparable to fSWb-2.

3.4.3. fSWc units

fSWc-1: radar-intermediate to radar-bright flow lobes partially covered by fSWc-3. Their terminations are not recognizable due to disruption by a craterless blast halo caused by an airburst of an incoming

bolide (cf. Antropova et al., 2023). These flows outcrop over an area of ~3500 km^2 and are assumed to be sourced from the summit, yielding an approximate flow length of ~390 km.

fSWc-2: radar-intermediate flows that partially cover fSWc-1 and are partially covered by fSWc-3 and fSWc-4. They occupy an area of ~2200 km^2 and have an estimated length of ~300 km, assuming they are sourced from the summit region or along its margin.

fSWc-3: radar-intermediate to radar-dark flows that partially cover fSWc-1 and fSWc-2, while being partially covered by fSWc-4 and fEb-3. They occupy an area of 4600 km^2 and have an approximate length of ~300–320 km, if sourced from the summit or its margin.

fSWc-4: radar-bright lobes radially spreading from an assumed flank source. They occupy an area of ~8700 km^2 and have an approximate length of ~300 km. These flows partially cover fSWb-2, fSWb-5, fSWc-2, and fSWc-3, while being crosscut by fSWc-5, fSWc-6, and fSWc-7. Changes in trend of some of the flow lobes are associated with topographic highs from pre-Atira Mons material.

fSWc-5: distinctive radar-bright flow lobes sourced from the summit region. They cover an area of ~4000 km^2 and have an estimated length of ~150 km. They crosscut fSWc-4 and fEa-1, and are partially covered by fSWc-6, fSWc-7, and fEb-3.

fSWc-6: radially spreading narrow radar-bright lobes associated with the same flank source as fSWb-2 and fSWb-5. They partially cover fSWb-2, fSWb-5, and fSWc-4, and are partially covered by fSWc-6. They occupy an area of ~3600 km^2 and have a maximum length of ~145 km.

fSWc-7: pervasive radar-dark flows sourced from the summit that cut older flows from units fW-1, fSWc-4, fSWc-5, fSWc-6, fEa-1, fEb-3, fSWa-2, fSWa-3, fSWb-2, and fSWb-5, while being partially covered by fSWc-8 and fEd-2. They occupy an area of ~16,300 km^2 and have a maximum length of ~260 km.

fSWc-8: radar-dark flows that occupy a small area of ~600 km^2 near Atira Mons' summit. They crosscut fSmt-1 and fSWa-2, while being partially covered by gSmt-1.

3.5. Northern units (N)

The geological maps of northern flow packages "a" and "b" are displayed on Figs. 13 and 14, respectively. General location of the area can be seen on Fig. 7.

3.5.1. fNa units

fNa-1: radar-dark flow lobes crosscut by fNb-3, fNb-4, fNb-5, and fNa-5. They cover an area of ~1100 km^2 and having a maximum length of ~70 km. Lobes diverging from a single spot indicate a possible flank source.

fNa-2: radially spreading radar-bright flow lobes, whose source appears to converge to the summit. They occupy an area of ~2800 km^2 and have a maximum length of ~180 km. They are crosscut by fNa-5, fNb-3, fNb-5, and fNb-6.

fNa-3: radar-intermediate to radar-bright patches that are crosscut by fNa-5, fNa-7, fNa-8, and fNa-9. They are exposed over an area of ~1700 km^2. Their source appears to be the same flank vent that supplied lava to fNa-7 and fNa-9, yielding a maximum length of ~150 km.

fNa-4: radar-intermediate to radar-dark flows that occupy the northeastern portion of Atira Mons, with flow boundaries that tend to be more radar-bright than their core. They cover an area of ~2700 km^2 and have a maximum length of ~100 km, assuming a flank vent as the source. They crosscut fEb-1 and are crosscut by fEb-3, fNa-5, fNb-1, and fNb-5.

fNa-5: summit-sourced radar-intermediate flow unit that is the most widespread on the northern portion of Atira Mons, creating an apron of ~29,600 km^2 and having a maximum length of ~230 km. It partially covers fNa-1, fNa-2, fNa-3, fNa-4, fEb-1, and fEb-3, and is crosscut by fNa-7, fNb-1, fNb-2, fNb-3, fNb-4, fNb-5, fNb-6.

fNa-6: set of radar-intermediate flow lobes that are sourced from the summit region, cover an area of ~3100 km^2 and have a length of ~160

Fig. 11. SAR image (top) and geologic map (bottom) of the southwestern flow package "b". Green line marks Atira Mons' outer boundary. Geological units are described in the text and Table B1 (Appendix B).
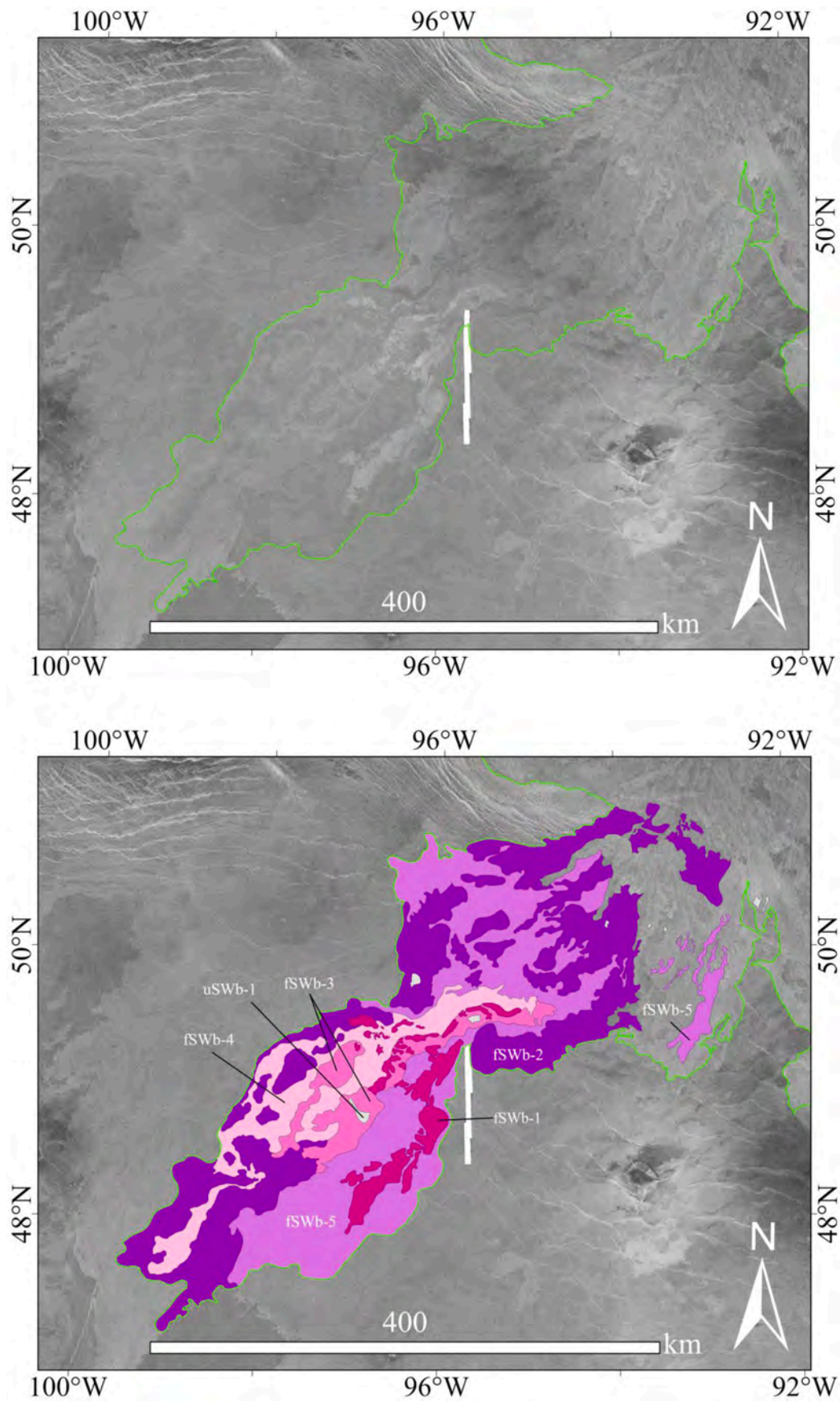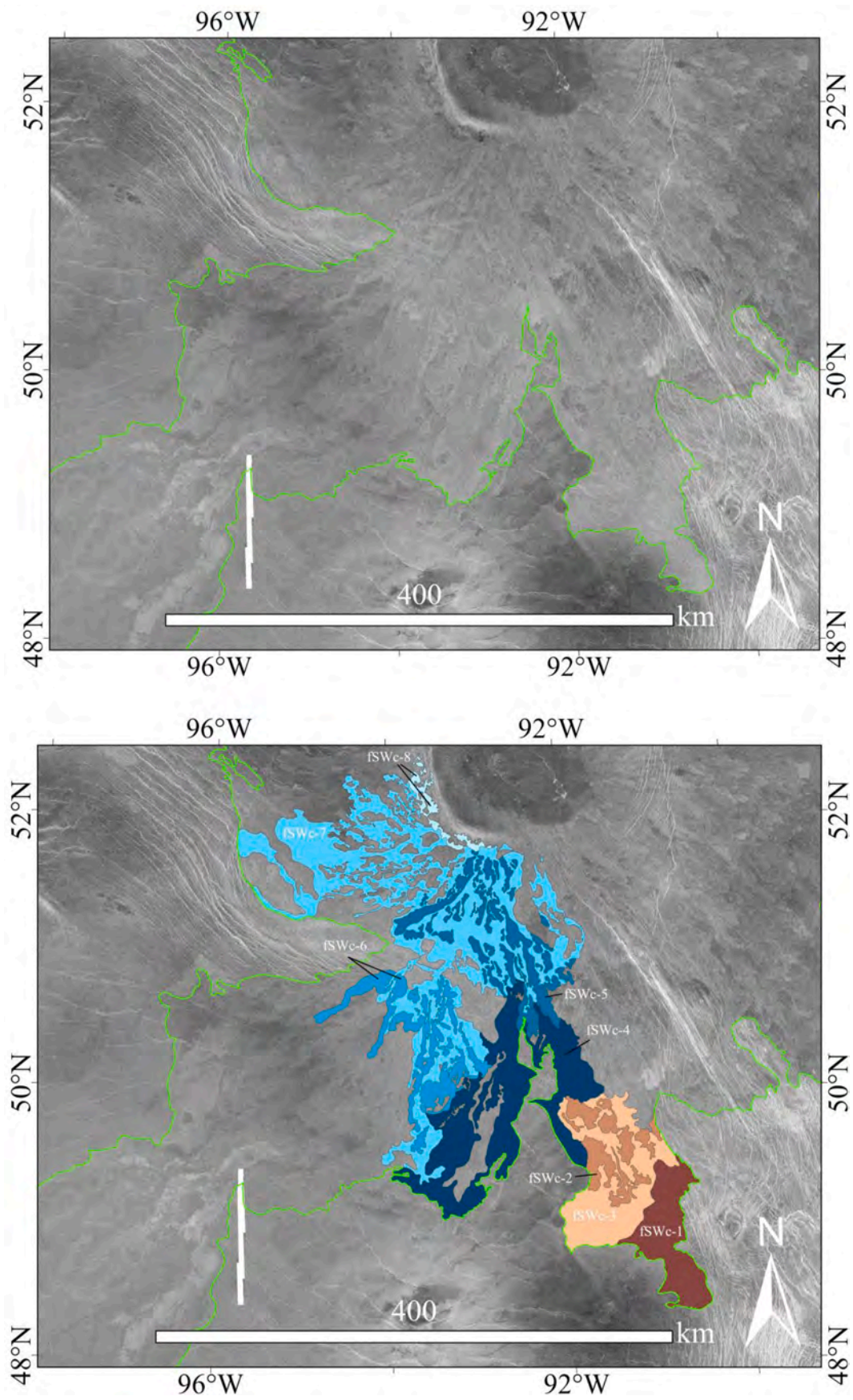
Fig. 12. SAR image (top) and geologic map (bottom) of the southwestern flow package "c". Green line marks Atira Mons' outer boundary. Geological units are described in the text and Table B1 (Appendix B).

Fig. 13. SAR image (top) and geologic map (bottom) of the northern flow package "a". Green line marks Atira Mons' outer boundary. Geological units are described in the text and Table B1 (Appendix B).

Fig. 14. SAR image (top) and geologic map (bottom) of the northern flow package "b". Green line marks Atira Mons' outer boundary. Geological units are described in the text and Table B1 (Appendix B).
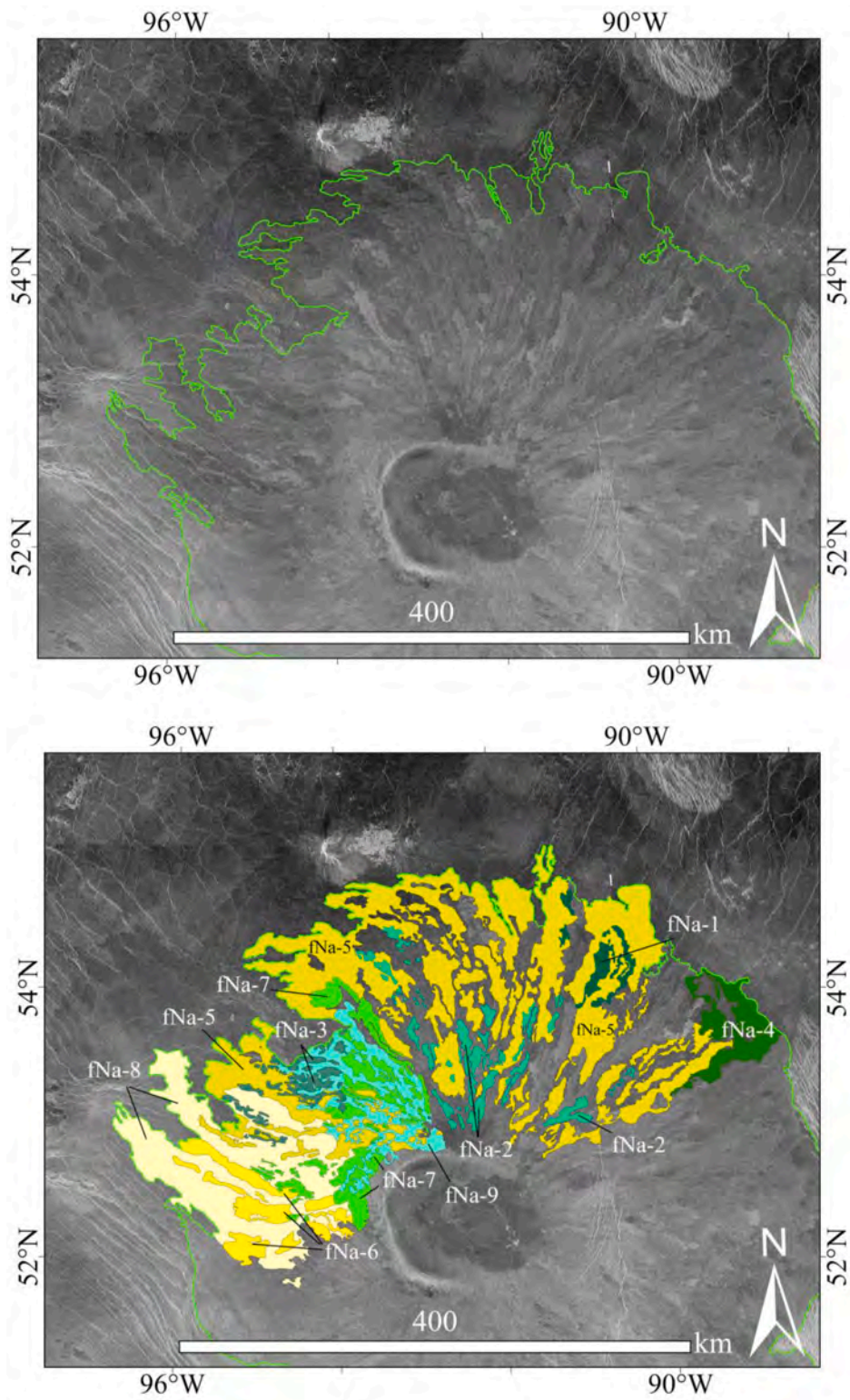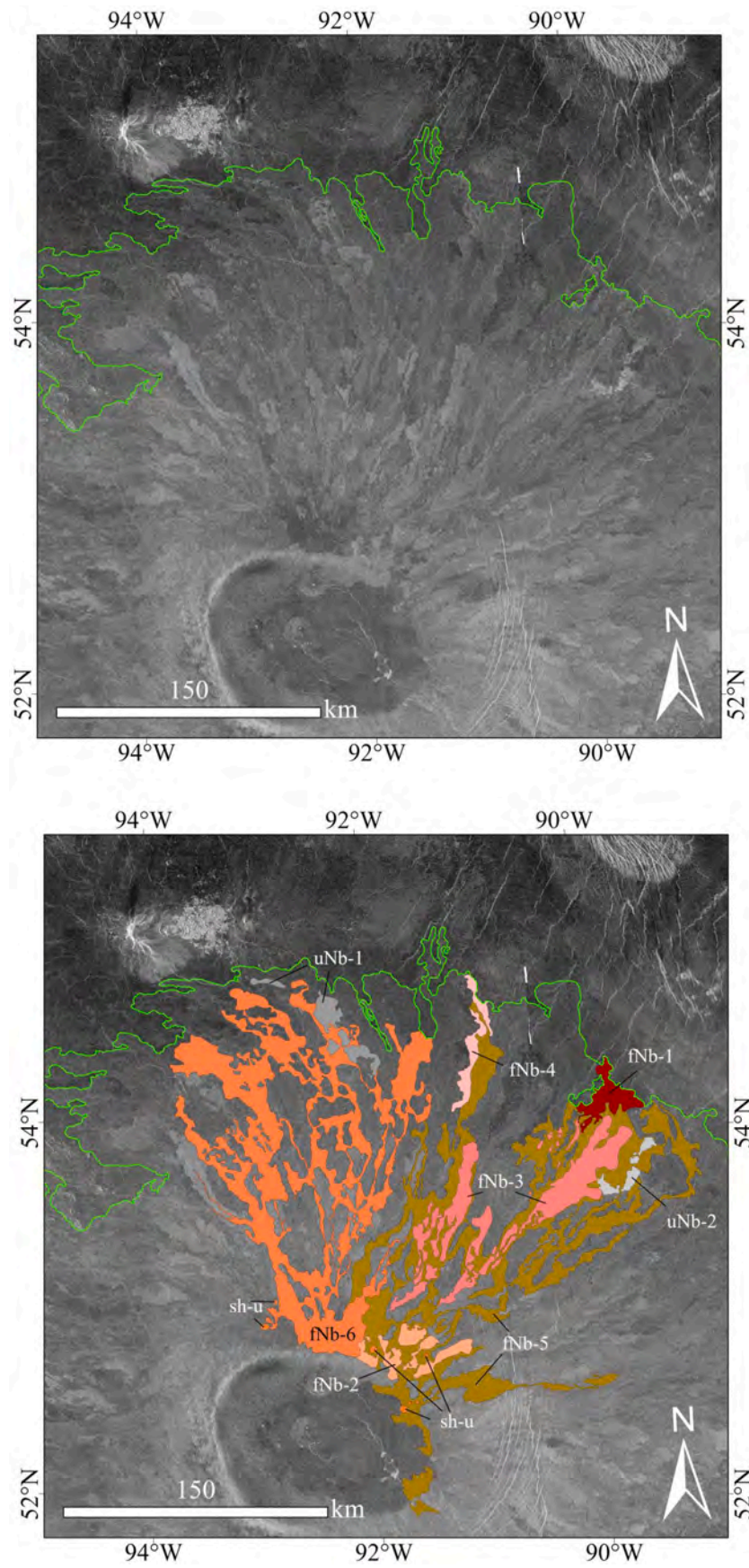
km. These flows are crosscut by fNa-7, fNa-8, and fSWc-7, and partially cover fW-1. Together with fNa-8 these flows appear to be influenced by the presence of regional wrinkle ridges on the northwestern portion of Atira Mons, indicating that they formed after the deformation event that created these regional structures.

fNa-7: radar-bright flow lobes that originate from a flank source near Atira Mons' summit, occupy an area of ~4300 km^2 and have a length of ~140 km. They crosscut fNa-5 and fNa-6 and are partially covered by fNa-9 and fNb-6.

fNa-8: pervasive radar-dark flow lobes that appear to be sourced from the summit, cover an area of ~11,200 km^2 and have a length of ~200 km. Together with fNa-6, they appear to be influenced by a set of regional wrinkle ridges on the northwestern portion of Atira Mons.

fNa-9: radially spreading radar-dark flows that are sourced from the same flank source as fNa-7, occupy an area of ~4200 km^2 and have a length of ~130 km. They crosscut fNa-7, fNa-5, fNa-3, gSmt-1 and are partially covered by fNb-6.

3.5.2. fNb units

fNb-1: radar-dark flow with distinctive radar-bright boundaries located on Atira Mons northeastern portion. It partially covers fNa-4 and fNa-5 and is crosscut by fNb-5. Judging by the preservation of flow lobes, its source should be a flank vent, which yields a length of ~45 km and an exposed area of 500 km^2.

fNb-2: radar-intermediate to radar-bright short flow lobes sourced from the summit. Crosscuts fNa-5 and is crosscut by fNb-5. They occupy an area of ~700 km^2 and have an approximate length of ~35 km.

fNb-3: set of prominent radar-bright flow lobes that show evidence of lava breakouts (e.g., Walker, 1971; Head et al., 1993; Blake and Bruno, 2000). They cover an area of ~2600 km^2 and have a maximum length of ~210 km. They crosscut fNa-1, fNa-2, and fNa-5, while being partially covered by fNb-5. Judging by the radial spread from a single spot, a flank vent is assumed.

fNb-4: isolated radar-intermediate to radar-bright flow lobe sourced from a flank vent. It crosscuts fNa-1 and fNa-5 and is partially covered by fNb-5. It has a maximum length of ~75 km and an exposed area of ~400 km^2.

fNb-5: radar-dark flow lobes sourced from vents on the northeastern portion of Atira Mons' summit. They cover an area of ~9200 km^2 and have a length of ~215 km. They crosscut fSmt-1, fNb-1, fNb-2, fNb-3, fNb-4, fNa-1, fEb-3, and fEd-1 and are partially covered by fNb-6.

fNb-6: radar-dark flow lobes sourced from the northern portion of Atira Mons' summit. They crosscut fNa-2, fNa-5, fNa-7, fNa-9, and fNb-5 and are among the youngest units of Atira Mons. Flows from this unit cover ~9000 km^2 and have a maximum length of ~130 km.

3.6. Eastern units (E)

The geological maps of eastern flow packages "a", "b", "c" and "d" are displayed on Figs. 15–18, respectively. A general location of the area can be seen on Fig. 7.

3.6.1. fEa units

fEa-1: radar-dark patches pertaining to older stages of Atira Mons' visible history. They are located mainly around rdgEa-1. They are exposed in an area of ~6700 km^2, having maximum length of ~220 km. Due to proximity of the summit region and widespread distribution they are assumed to be sourced from there.

fEa-2: patches and lobes of radar-bright flows sourced from Atira Mons' summit region. They occupy an area of ~3500 km^2 and have an approximate length of ~270 km. They are crosscut by fEb-3, fEb-5, fEc-5, fEd-3, and fEd-2 and partially cover fEa-1 and fEc-4.

3.6.2. fEb units

fEb-1: radar-dark patches occupying Atira Mons eastern periphery. They are partially covered by fEb-3, fEc-5, and fEa-2. These flows are

assumed to be sourced from the summit and cover an area of ~4900 km^2, having a maximum length of ~260 km.

fEb-2: narrow and relatively short patches of radar-bright lavas. They could be sourced from the summit, but the linear boundary of one of the flows suggest that the source could be an underlying dyke or dykes associated with the arcuate fractures sAF-2 (see Section 5.3). This unit occupies an area of ~800 km^2 and extends for a length of ~120 km. These flows are crosscut by fEb-3, fEb-4, fNa-2, fNa-5, and fNb-5.

fEb-3: the most widespread unit of Atira Mons' eastern flank is composed of a multitude of radar-intermediate lobes that originate from the summit, form an apron that covers an area of ~37,600 km^2 and have a maximum length of ~250 km. These flows crosscut fNa-4, fNb-5, fEb-1, fEb-2, fEa-1, fEa-2, fSWc-2, fSWc-3, and fSWc-4, and are partially covered by fSWc-7, fEb-4, fEb-5, fEc-5, fEc-6, fEd-1, fEd-2, and fEd-3.

fEb-4: radar-dark flows that form a narrow lobe, which is sourced from an assumed flank vent on Atira Mons' northeast, or perhaps from an underlying dyke as suggested for fEb-2 (see Section 5.3). They crosscut fEb-2, and fEb-3 and are partially covered by fNb-5, They extend over an area of 1000 km^2 and have a maximum length of ~100 km.

fEb-5: radar-dark flows that emanate from fractures on Atira Mons' southeast. They cover an area of ~400 km^2 and have a maximum length of ~65 km. They crosscut fEb-3, fEa-1, and fEa-2.

3.6.3. fEc units

fEc-1: isolated radar-intermediate patches on Atira Mons southeastern flank. They occupy an area of ~1000 km^2 and have an estimated length of ~330 km, assuming a summit source. They are partially covered by fEc-2 and fEc-4.

fEc-2: radar-intermediate to radar-dark flows surrounding Davies Patera (see Fig. 4a) and crosscutting fEc-1, while being partially covered by fEc-3 and fEc-4. They cover an area of ~3200 km^2 and have an estimated length of ~415 km, assuming a summit source.

fEc-3: radar-dark flows with radar-bright boundaries. They partially cover fEc-2 and are partially covered by fEc-4. They occupy an area of ~700 km^2 and have an approximate length of ~270 km, assuming a summit source.

fEc-4: radar-intermediate to radar-bright flows with rougher boundaries. They partially cover fEc-3, fEc-2, and fEc-1, while being crosscut by fEc-5. These flows occupy an area of ~3800 km^2 and have a length of ~305 km, assuming a summit source or one along its margins.

fEc-5: young radar-dark flows that appear to emanate from the arcuate fractures (sAF-2) on Atira Mons' eastern flank (see Section 5.3). They crosscut fEb-1, fEb-3, fEa-1, fEa-2, and fEc-4 and are partially covered by fEc-6. They extend over an area of ~9600 km^2 and have an approximate length of ~270 km.

fEc-6: two radar-intermediate to radar-bright flows that also seem to emanate from the arcuate fracture system (sAF-2) on the eastern flank of Atira Mons (see Section 5.3). They occupy an area of ~380 km^2 and have a maximum length of ~65 km. They crosscut fEb-3 and fEc-5.

3.6.4. fEd units

fEd-1: summit sourced radar-bright to radar-intermediate flow lobe. It occupies an area of ~320 km^2 and has a maximum length of ~60 km. It partially covers fEb-3 and is crosscut by fNb-5 and fEd-2.

fEd-2: radar-intermediate flows sourced from the summit that cover an area of ~2300 km^2 and have a maximum length of ~90 km. They crosscut fEd-1, fEa-2, and fNb-5, while being crosscut by fEd-3.

fEd-3: radar-dark flows that crosscut fEd-1, fEd-2, fEa-2, and fNb-5. They occupy an area of ~2500 km^2 and have a length of ~200 km. This is one of the youngest units on Atira Mons.

3.7. Western units (W)

The geological map of the western flow package is displayed on Fig. 19. A general map showing the area's location can be seen on Fig. 7.

Fig. 15. SAR image (top) and geologic map (bottom) of the eastern flow package "a". Green line marks Atira Mons' outer boundary. Geological units are described in the text and Table B1 (Appendix B).

Fig. 16. SAR image (top) and geologic map (bottom) of the eastern flow package "b". Green line marks Atira Mons' outer boundary. Geological units are described in the text and Table B1 (Appendix B).
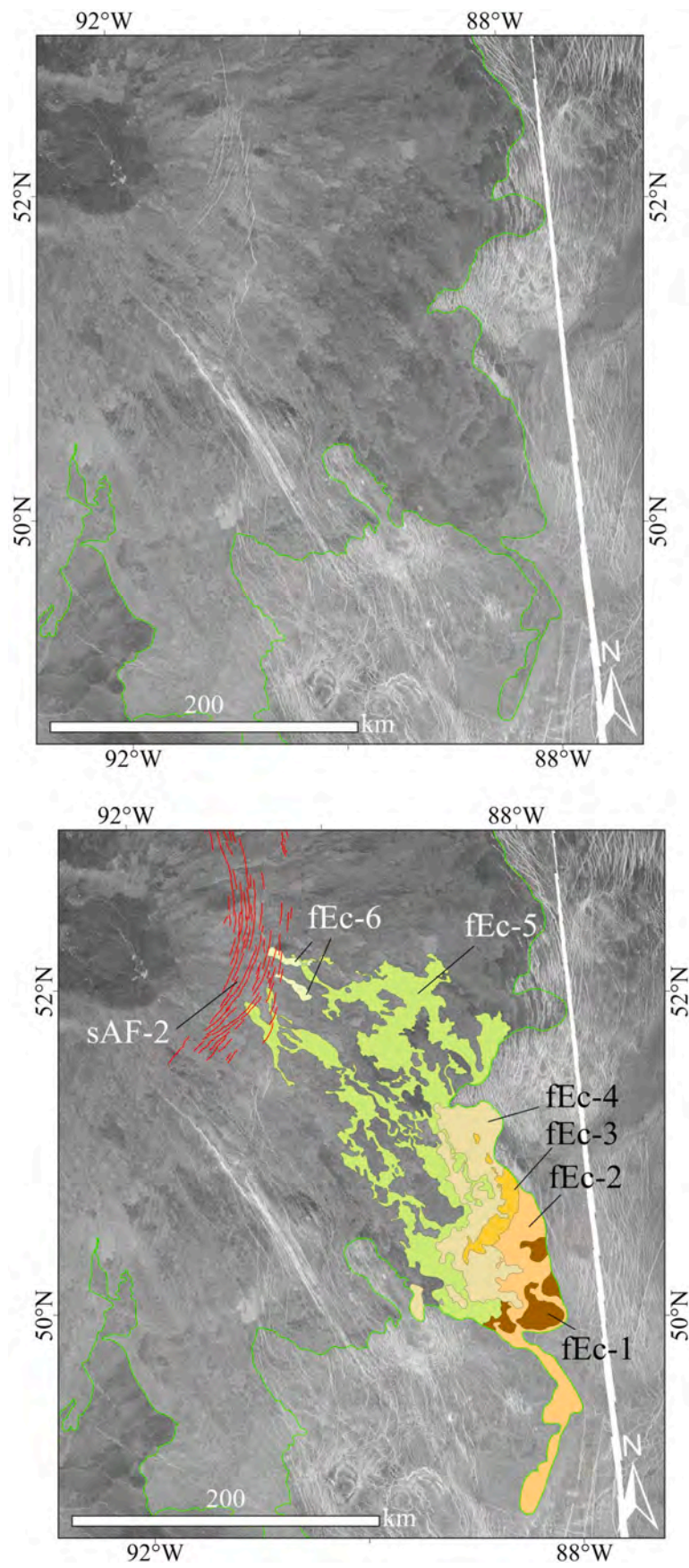
Fig. 17. SAR image (top) and geologic map (bottom) of the eastern flow package "c". Green line marks Atira Mons' outer boundary. Geological units are described in the text and Table B1 (Appendix B).
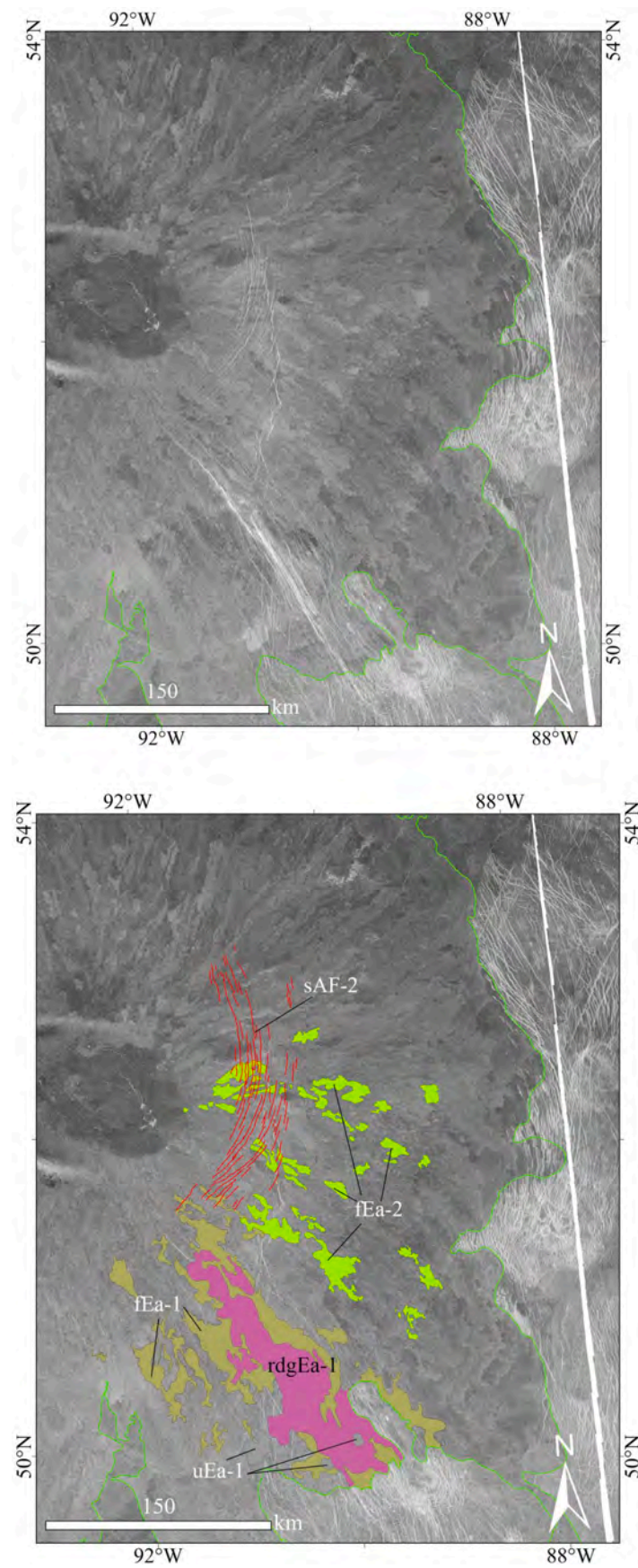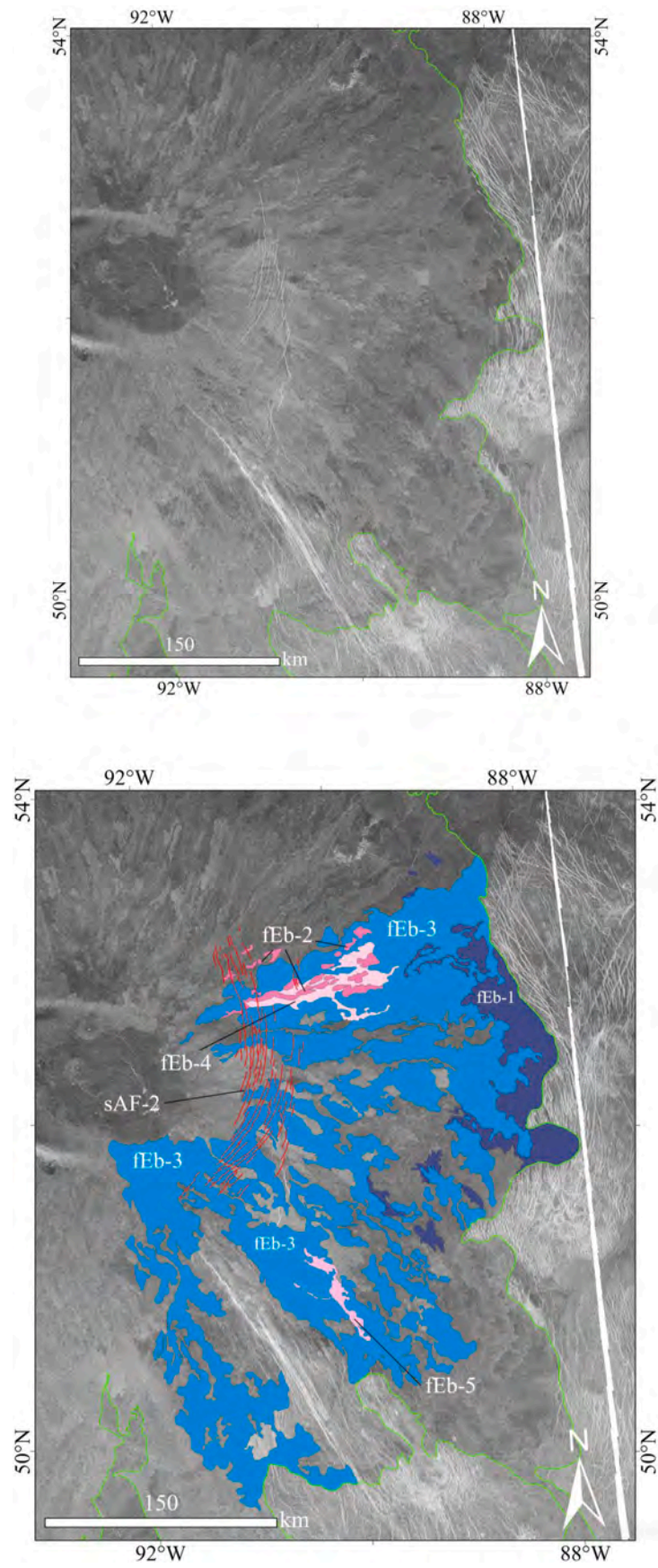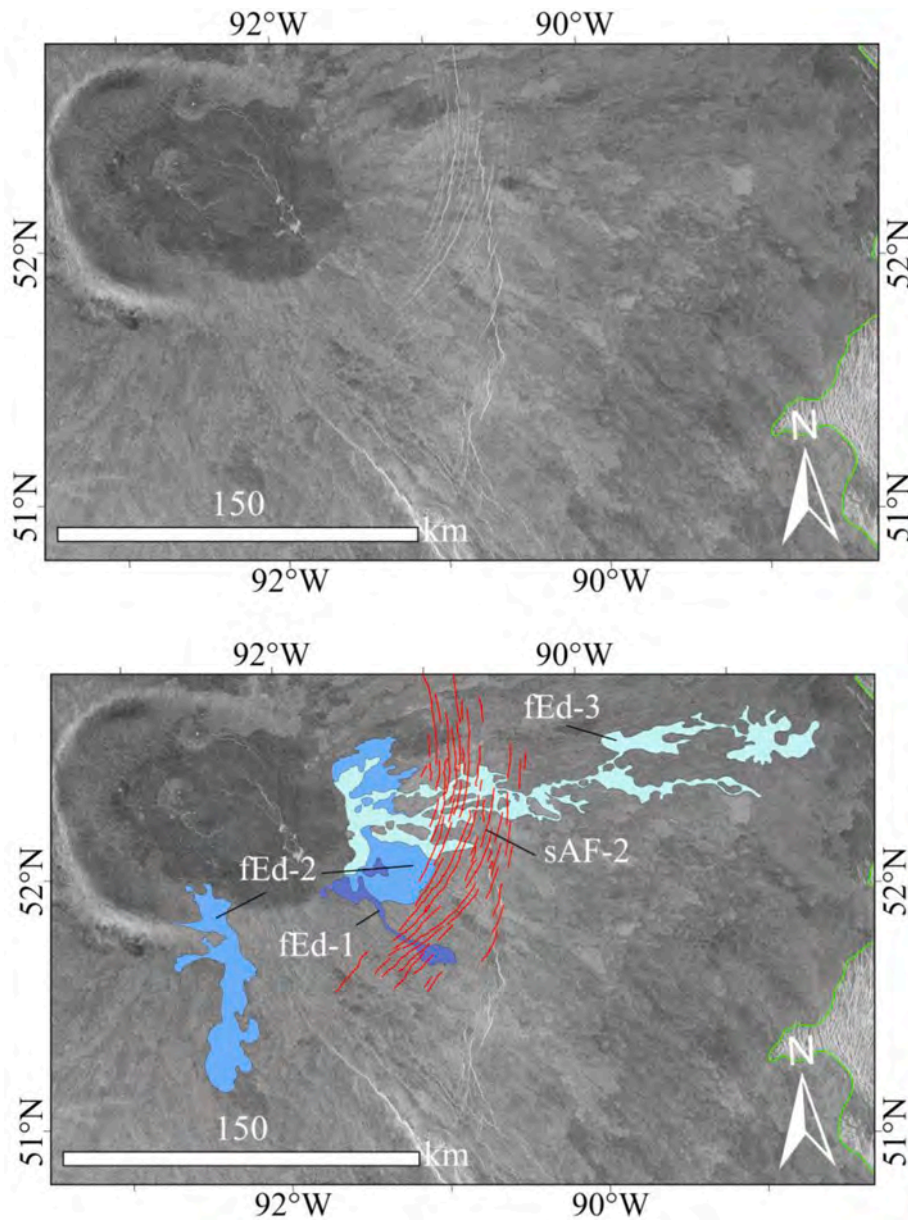
Fig. 18. SAR image (top) and geologic map (bottom) of the eastern flow package "d". Green line marks Atira Mons' outer boundary. Geological units are described in the text and Table B1 (Appendix B).

fW-1: radar-intermediate flows with diffuse boundaries that are the oldest units on the western flank of Atira Mons. Their limits coincide with a topographic high that is marked by a set of arcuate fractures. These flows occupy an area of ~3000 km^2 and have a maximum length of ~200 km. Sources for this flow unit are not seen. The flows are crosscut by fNa-8, fNa-6, and fWc-7.

3.8. Structural units

sAF-1: a minor set of arcuate fractures crosscutting fSmt-2, located on the western portion of Atira Mons' summit (Fig. 9). Fractures vary in length from ~3 to ~10 km. If this system forms a full circumference, its maximum diameter is ~270 km.

sAF-2: a major set of arcuate fractures that dominates Atira Mons' eastern flank (sAF-2, Figs. 15–18) and seems to be the source for some of the flows (e.g., fEc-5, fEc-6). If it forms a full circumference, this major system has a maximum diameter of ~350 km, and has fractures ranging in length from a few kilometers to ~150 km. Its age relative to other

flows is complex and the system appears to consist of several generations of fractures (see Section 5.3).

sPF: polygonal fractures that dominate the western portion of Atira Mons' summit (Fig. 9). They are mainly correlated with unit fSmt-2 and range in length from a few kilometers to ~70 km.

sWR: wrinkle ridges that mainly deform fSmt-3 (Fig. 9). They vary in length from a few kilometers to ~40 km.

3.9. Other units

rdgEa-1: structural-material unit (Ivanov and Head, 2011) that consists of volcanic material that forms a densely fractured ridge on the southeast of Atira Mons' summit. This unit consists of an assemblage of volcanic units that were intensely deformed and masks the underlying material in the resolution of the available dataset. It is partially covered by fEb-3 and fEa-1. The ridge is exposed on an area of ~5300 km^2.

sh-u: undivided shield volcanoes that have uncertain age relationships with the other Atira Mons-related units.

Fig. 19. SAR image (top) and geologic map (bottom) of the western flow package. Green line marks Atira Mons' outer boundary. Geological units are described in the text and Table B1 (Appendix B).
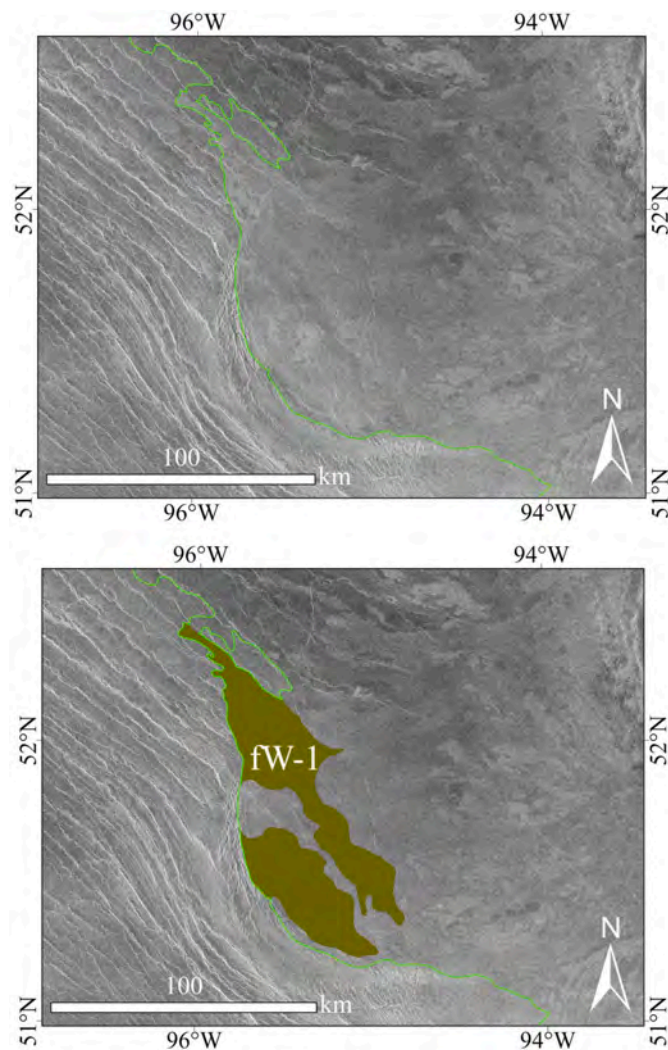
uSmt-1: radar bright patches on Atira Mons' summit associated with sWR. They could be remnants of Atira Mons' buried rim. They cover an area of ~35 km^2.

uSWb-1: isolated and irregular patches of radar-dark material with uncertain origin. They occupy an area of ~280 km^2.

uEa-1: isolated and irregular patches of radar-bright material of uncertain origin that occupy an area of ~400 km^2.

uNb-1: radar-bright material with a distinctive patchy signature in the radar images. It lacks the typical lobate appearance of lava flows, being more like other landslides on Venus (Ford et al., 1993). The lack of higher resolution topographic data hampers the identification of this unit which occupies an area of ~220 km^2.

uNb-2: isolated radar-bright patches that could be older units related to Atira Mons' initial stages or lava breakouts associated with younger flows. This unit occupies an area of ~520 km^2.

4. Stratigraphy

The stratigraphic relationships between Atira Mons's geologic units are summarized in Fig. 20, based on the discussion of age packages and cross-cutting relationships in the previous section. Six flow stages (and some sub-stages) are suggested by this analysis. The units belonging to each stage are listed in Table 1:

5. Discussion

5.1. Exposed geological history

The data were divided into columns in Fig. 20 based on the different sectors mapped. The tie lines identify a number of cross-cutting relationships revealed across the different sectors. This indicates that there are separate volcanic stages in which the flows on multiple sides of the volcano were emplaced at about the same time. Classification of volcanic stages in terrestrial LIPs into chemostratigraphic packages is based on volcanological, stratigraphic and chemical evidence (e.g., Jerram and Widdowson, 2005; Lightfoot and Keays, 2005; Rooney, 2017). Although flow morphology, geomorphology, radar-surface interactions, and cross-cutting and embayment relationships account for the volcanological and stratigraphic aspects of applying this approach to the Venusian surface, the chemical data provides only generalizations based on the Venera and VeGa datasets (e.g., Kargel et al., 1993) and petrological modelling (e.g., Shellnutt, 2013). Therefore, the recognition of multiple horizontal links correlating different flow packages only allow us to provisionally identify the temporal evolution of the mapped units of Atira Mons in six different stages (Figs. 20 and 21, Table 1).

Stage 1 is characterized by a high volume of flows exposed over an area of ~91,170 km^2 (~30.6% of the total area) and represents the initial eruption episodes of Atira Mons' mapped history. Geographically, these units are restricted to the volcano's southwestern and southern flanks, and form Atira Mons' longest flows that extend ~700 km from the present summit (fSWb-4 and fSWb-5, Fig. 11). This suggests high initial effusion rates (e.g., Walker, 1973; Harris and Rowland, 2009; Head and Wilson, 1986; Magee Roberts and Head, 1993; Magee and Head, 1995), which are consistent with terrestrial rift zone eruptions (e. g. 2018 Kilauea East Rift Zone eruption; Dietterich et al., 2021). The change in width of units of flow package SWb down slope, and the fact that their flow direction seems to be influenced by preexisting regional topographic barriers (e.g., rdg, Fig. 4), indicates that the current underlying topography does not differ significantly from the topography when the flows were initially emplaced. In terms of sources, flank eruptions are observed for some flow packages (fSWb-1, fSWb-3, fSWb-4), while summit sources are possible, but not confirmed, for others (fSWb-2, fSWb-5). Additionally, this stage contains the structural material unit rdgEa-1, a densely fractured unit that could contain early pre- or syntectonic volcanic material genetically associated with Atira Mons, as well as older geologic units associated with the corona cluster (ccl, Fig. 4), which includes Davies Patera.

Stage 2 is also characterized by a high volume of flows, currently exposed over an area of 63,741.1 km^2 (21.4% of the total area). In contrast to Stage 1, these flows are predominantly summit-sourced and are almost entirely restricted to the eastern flank of the volcano, although isolated patches can be seen on the northwestern and northern flanks. The distribution of these flows leads to two different hypotheses: a) the flow apron's boundary coincides with the terminations of the C-shaped high relief rim (fSmt-1; Fig. 9) that bounds the asymmetrical summit caldera. If flows from Stage 2 are burying the eastern portion of the rim, this could constrain the age of fSmt-1 to a period before the emplacement of Stage 2 flows; or b) the flow apron spanned a larger portion of the volcano (as suggested by fNa-1 and fNa-2) but was overlain by flows of subsequent stages. Lastly, Stage 2 partially surrounds the ridge included in rdgEa-1 and flows towards the topographic low of the corona cluster (ccl, Fig. 4), while ponding on the slopes of the eastern groove belts (gb, Fig. 4).

The last high-volume episode of Atira Mons' evolution is Stage 3, exposed over an area of 85,793.8 km^2 (28.8% of the total area). This stage forms most of the western flank, as well as significant parts of the northern, eastern, and southern flanks. Again, most flows are sourced from the summit or near-summit regions. However, multiple flank-sourced flows are also emplaced (e.g., fSwc-4, fSWc-6, fEc-5, fNa-7). Of these, all are associated with point sources, except fEc-5. This last unit
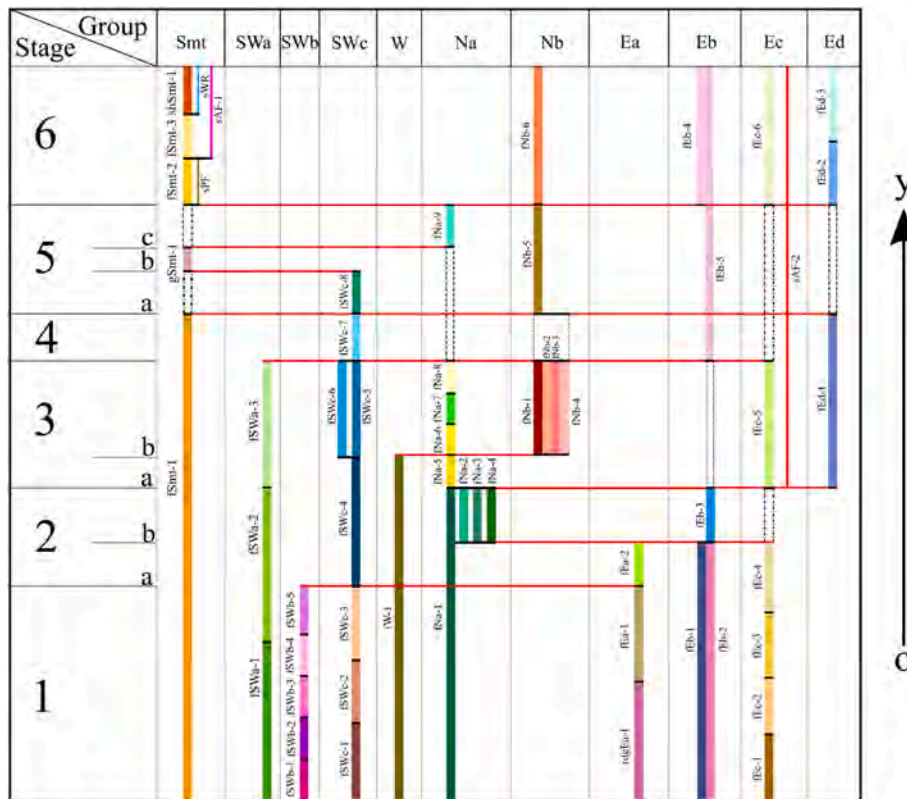
Fig. 20. Relative age relationships between Atira Mons' units. Black lines – true contacts between units in a flow group; red lines – true contacts between flow groups; dotted lines – clear relationship in a group and unclear relationship between groups. Arrow points in younging direction ("o" is old and "y" is young).

Table 1
Atira Mons' stages, their respective units and areal distribution.

Stage	Units	Exposed area (km^2); % of total area
1	fSWb-1, fSWb-2, fSWb-3, fSWb-4, fSWb-5 fSWc-1, fSWc-2, fSWc-3, fEa-1, rdgEa-1	91,172.3; 30.6
2a	fEa-2, fEb-1, fEb-2, fEc-1, fEc-2, fEc-3, fEc-4	63,741.1; 21.4
2b	fNa-1, fNa-2, fNa-3, fNa-4, fEb-3	
3a	fW-1, fNa-5, fSWc-4	85,793.8; 28.8
3b	fSWa-1, fSWa-2, fSWa-3, fSWc-5, fSWc-6 fNa-6, fNa-7, fNa-8 fNb-1, fNb-2, fNb-3, fNb-4, fEc-5	
4	fSWc-7, fEd-1, fSmt-1	18,474.8; 6.2
5	fSWc-8, gSmt-1, fNa-9, fNb-5,	14,739.3; 4.9
6	fSmt-2, fSmt-3, shSmt-1, fNb-6, fEb-4, fEb-5, fEc-6, fEd-2, fEd-3, sPF, sWR, sAF-1, sAF-2	24,014.4; 8.1

appears to originate from the eastern arcuate fracture system (sAF-2), indicating that the fractures could overlie dykes (see Section 5.3). This puts a lower constraint on the age of at least some of these fractures. Lastly, the deformed basin (db, Fig. 4) in the northwest controls the swinging of north-trending flows to the northwest and of west-trending flows to the north. This is further evidence that the regional topography has not changed significantly after Atira Mons' buildup.

Stage 4 involves a massive reduction in lava output, judging by its exposed area of only 18,474.8 km^2 (6.2% of total area). Flows are all sourced from the summit region. On the south and southwest they are almost exclusively represented by highly channelized radar-dark flows (fSWc-7), while on the east there is an individual ~60 km-long flow lobe (fEd-1). Geologically, the most significant information derived from this stage is an upper age constraint on Atira Mons' current rim (fSmt-1), which is partially covered by flows from Stages 5 and 6.

The penultimate stage of Atira Mons' evolution, Stage 5, covers an area of 14,739.3 km^2 (4.9% of total area). It consists of narrow, long,

radar-dark channelized flows sourced from the summit (e.g., fNb-5) or from flank sources near the summit (e.g., fNa-9), Additional units include mass wasting products (gSmt-1) of the rim (fSmt-1), providing a time constraint linking the flank flows on the west and northwest to the caldera collapse event.

Stage 6 concludes the visible eruption history of the Atira Mons shield volcano. It covers an area of 24,014.4 km^2 (8.1% of the total area). fSmt-2 and fSmt-3 fill Atira Mons' caldera (see Section 5.2), probably sourced from the multiple vents and shield volcanoes (shSmt-1; Fig. 9) of the summit region. These shield volcanoes are evidence of resurgence, something commonly observed on Earth on silicic calderas, but rarely on mafic ones. Furthermore, parts of the flows filling the caldera appear to be flowing uphill, indicating subsidence with tilting of the area after their emplacement. Considering that on terrestrial volcanoes lateral magma migration is known to occur (e.g., Gundmundsson et al., 2016), a piston-like, down-sagging component for subsidence on the summit region could account for the multiple young flows that appear to be emanating from arcuate fractures on the east (fEb-5, fEb-4, fEc-6). Lastly, as with Stages 4 and 5, long and narrow channelized radar-dark units characterize the younger generations of flows forming the flanks of the volcano, in this case trending north and east.

In summary, the most voluminous flows are concentrated in the early stages (1–3) of Atira Mons' exposed history, while the younger pulses, with a few exceptions, are shorter and less voluminous (4–6), as illustrated in Figs. 21 and 22. The development of the summit region appears to be the closing episode of Atira Mons' activity, although some of the arcuate fractures cast doubt on this hypothesis (see Section 5.3). Furthermore, Atira Mons' growth was strongly influenced by the pre-existing regional topography, resulting in an asymmetrical edifice and outer flow apron, as evidenced by its shape and by the geographic distribution of flows over time. Changes in the topography of the volcano are mainly confined to the summit region and appear to be related to episodes of caldera subsidence, which may have first occurred before the
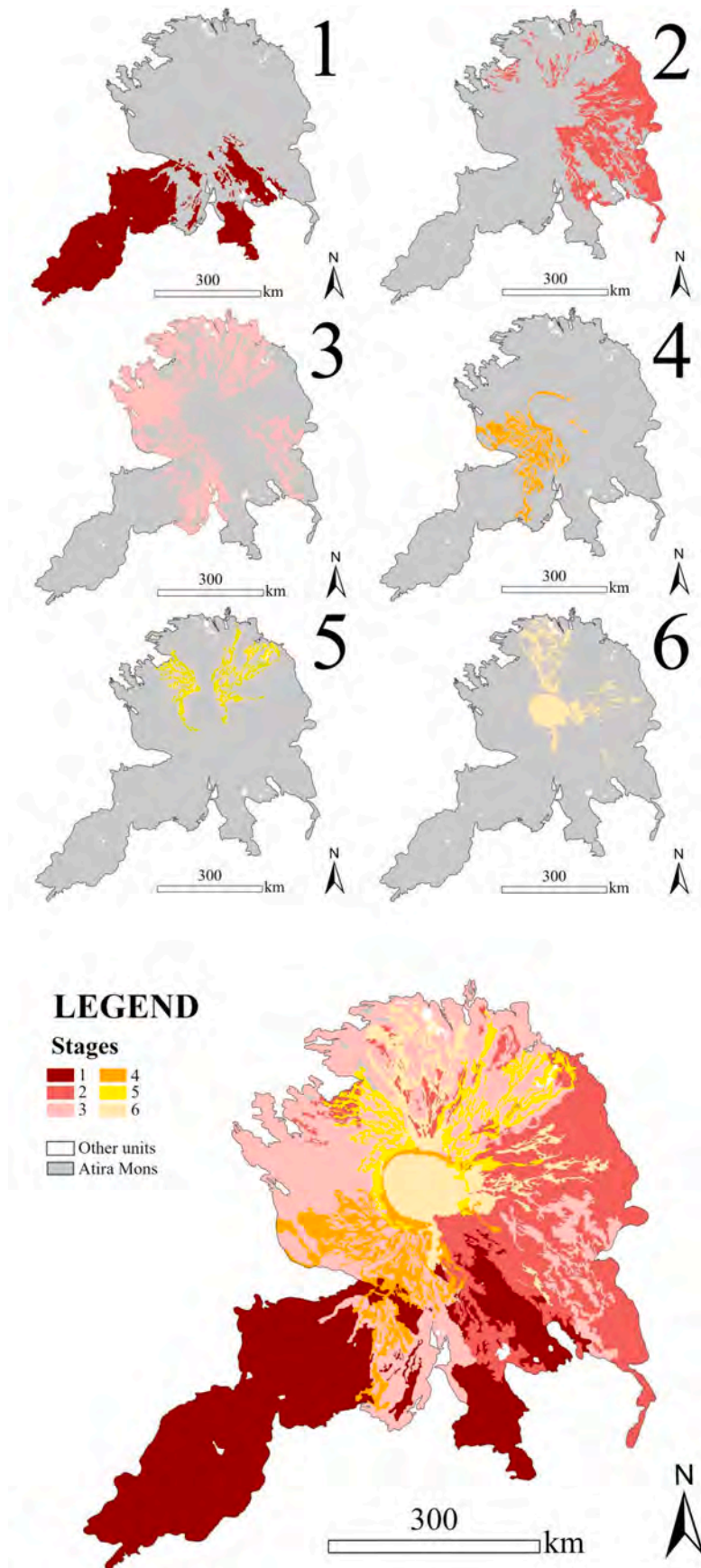
Fig. 21. Schematic representation of Atira Mons' volcanic stages depicted individually (top; 1–6) and generally (bottom).
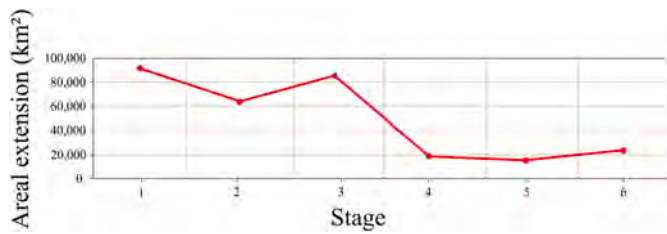
Fig. 22. Areal distribution of geologic units over time.

emplacement of Stage 2 or as late as Stage 4. Lastly, the arcuate fractures (sAF-2) that appear to be sources for some of the flows might have formed before or during Stage 3 and were periodically sources for lower volume flank flows.

5.2. Caldera morphology: associated mechanisms and causes

First of all, we consider what geological information Atira Mons' central caldera preserves. It is important to note that currently erosion plays a subordinate role on Venus (Campbell et al., 1997). Thus, calderas associated with the lobate plains (pl, Ivanov and Head, 2011), which form large shield volcanoes, are thought to retain their primary form and contain important information about the formation and structure of subsurface magma reservoirs (e.g. Head and Wilson, 1992). Indeed, some may still be active (Herrick and Hensley, 2023).

The Atira Mons caldera is comprised of the summit region units (Smt) (Fig. 9) and varies in diameter from ~115.8 to ~138.5 km. The dimensions of a caldera have been used as a proxy for the size of the underlying magma reservoir, with these dimensions implying the existence of a very large and shallow tabular magma chamber (Cole et al., 2005). Most Atira Mons flows can be traced back to sources on the summit or the near-summit region, namely groups i, j, k, l, m, n, and o (Fig. 8b; Table B2, Appendix B). Additionally, the summit is the region that contains the highest concentration of visible sources vents (Fig. 8a–Table B2, Appendix B). Older vents are assumed to be buried by younger flows, such as fSmt-2 and fSmt-3.

The morphology of the Atira Mons caldera is characterized by a topographically high C-shaped rim that is dominant on the western flank of the volcano but is not seen on the eastern flank (Fig. 5, W-E profile). At its highest point, on the western flank, the rim is ~1.1 km above the caldera's floor. The height of the western rim of the caldera and the small set of arcuate fractures cutting through fSmt-2 in that area suggests several episodes of buildup and successive collapses in the caldera. As with terrestrial volcanoes, such caldera collapse events on Venus are thought to be caused by the evacuation of a subsurface magma reservoir during large eruptive episodes, although other causes, such as inflation of the reservoir have been suggested (e.g., Gundmundsson, 1988).

If the topographic rim originally extended around the eastern side of the caldera to form a complete annular ring-fault zone, it can be inferred that it was then breached and covered by subsequent caldera-fed lava flows. Thus, Atira Mons' caldera morphology could reflect greater subsidence in the eastern portion of the caldera, caused by an asymmetric fault-bounded "trapdoor-like" mechanism (e.g., Heiken et al., 1986). Lipman (1997) showed that this morphology can be attributed to the existence of an asymmetric magma reservoir. Although there is no obvious effect of the volcano on the regional topography to point to this asymmetry, the volcano is more voluminous on the eastern flank, when compared to the western. This could be related to what is suggested by Varga and Smith, 1984, where such morphology is related to preferred magma withdrawal from one side of the caldera. Experimental studies (e.g., Roche et al., 2000) show that other factors could be responsible for asymmetric collapse, such as injection of magma and/or greater magma reservoir roof thickness. Additionally, the wrinkle ridges (sWR) that deform fSmt-3 (Fig. 9), are spatially correlated with a topographic low on the caldera's eastern side. This is consistent with a down-sagging

model, where compression occurs in the central area of a collapsed caldera roof (Branney, 1995). This has been observed on other volcanoes in the Solar System, such as Olympus Mons on Mars (Mouginis-Mark and Robinson, 1992). In summary, the Atira Mons summit preserves evidence of both down-sagging and trapdoor collapse.

Another important feature of Atira Mons' summit is evidence of resurgence, expressed as two young shield volcanoes (shSmt-1) emplaced inside the caldera (Fig. 9). This phenomenon is common for terrestrial silicic volcanoes, but rare on basaltic volcanoes (Trasatti et al., 2019). In Ischia, Italy, a silicic volcano with well documented resurgence exhibits a polygonal fracture pattern caused by the existence and reactivation of pre-collapse faults during resurgence (Acocella and Funiciello, 1999). One of the Atira Mons summit flows, fSmt-2, is visibly deformed by polygonal fractures, which are partially covered by younger fSmt-3 flows. Thus, the polygonal fractures on Atira Mons could document older episodes of resurgence, before the emplacement of fSmt-3. Additionally, the development of shield volcanoes late in Atira Mons' visible history is similar to shield volcano development during the waning phases of magmatism in the Yemen-Ethiopia flood basalt province (Kieffer et al., 2004).

Alternatively, the current morphology of Atira Mons' summit could be associated not with caldera collapse, but with sustained lava ponding favored by moderate to elevated confining pressures, shallow slopes, low volatile content in the lava, and moderate effusion rates (Clague et al., 2000). Terrestrial examples include the Halema'uma'u and Overlook craters at the summit of Kilauea (Patrick et al., 2018) and flat-topped cones of Niihau Island in the Hawaiian island chain (Cousens and Clague, 2015). In the case of Atira Mons, a lava lake >100 km across would have to grow and then be breached on its eastern flank to create the current topography of the volcano. Compared to these terrestrial analogues, Atira Mons' lava lake would need to have a diameter two orders of magnitude larger than, for instance, flat-topped cones on the Hawaiian island chain (maximum basal diameter of ~5 km; Clague et al., 2000), and its slopes would be much shallower (maximum slope of 7.5° at Atira Mons' summit compared with 25-30° slopes in shield stage flat-topped cones at the islands of Maui and Hawaii; Clague et al., 2000).

5.2.1. Volume of collapse

If we assume that a complete annular ring-fault zone formed during caldera collapse at the summit, we can estimate the minimum volume of flows that was erupted during that event by following the methodology
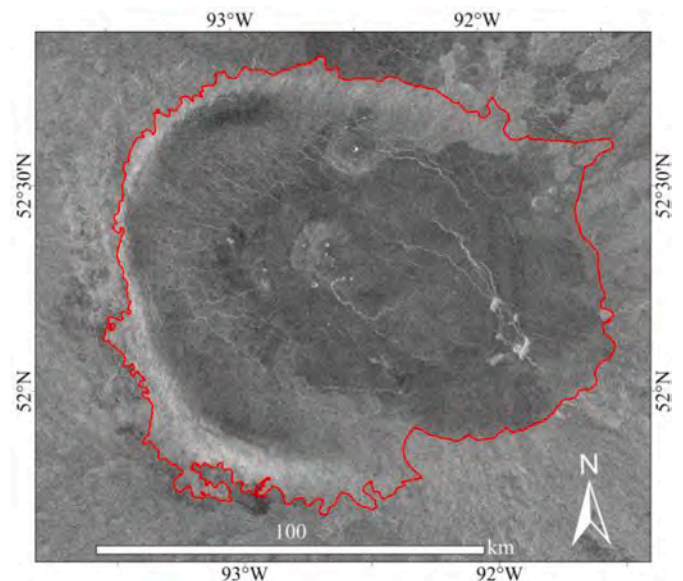

Fig. 23. SAR image of Atira Mons' summit caldera showing the inferred outline of the full annular rim.
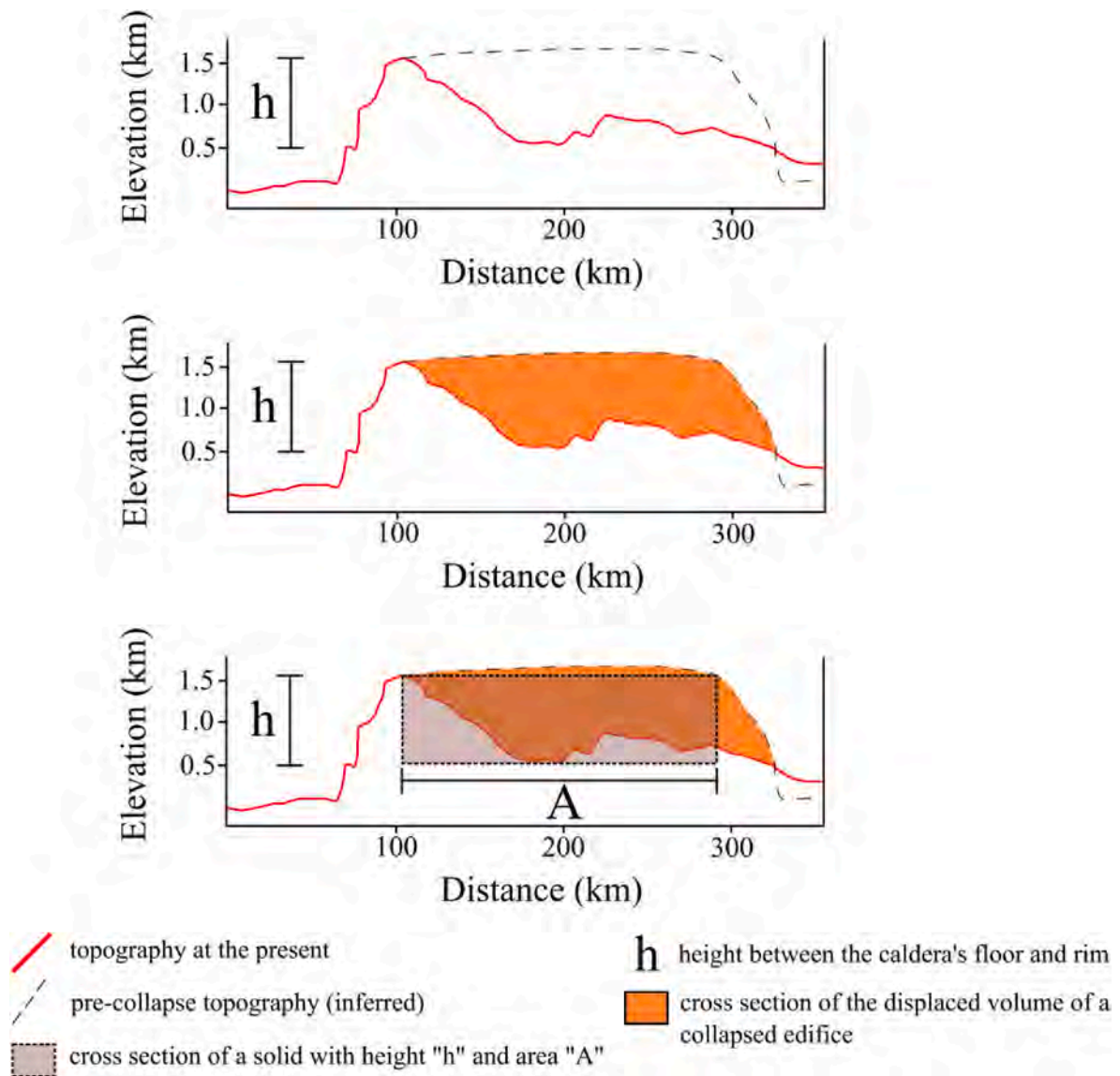
Fig. 24. Schematic representation of Atira Mons' caldera before collapse, outlining the approach to calculating the volume of flows necessary to accommodate the change in topography.

that is used to calculate the volume of the volcano (see details in Appendix A). The approach consists in first determining the inferred summit rim outline based on the topographic and radar data (Fig. 23). Then, the present volume of the region inside the rim (V_r) is calculated using the "Surface Volume" tool in ArcPro. Using the height between the roof of the caldera and the maximum height of the exposed rim (h) and the area inside the rim (A), one can estimate the volume of the original caldera (V_s). The volume of the collapsed portion of the caldera (V_c) is then determined by subtracting V_r from V_s (Fig. 24).

In our case:

$h = 1.1$ km

$A = 11,243.1$ km^2

$V_r = 6,877.3$ km^3

$V_s = A \bullet h$

$V_s = 12,367.4$ km^3

Therefore:

$V_c = V_s - V_r$

$V_c = 5,490.1$ km^3

Choosing flow thicknesses of 50 m (see "Discussion" in MacLellan et al., 2021) yields an areal extent (A_f) of:

$A_f = 109,802.0$ km^2

This analysis indicates that a cumulative collapse event could emplace a lava flow sheet 50 m thick over an area of about 1/3 of the whole volcano. This is consistent with the size of the volcano and with the idea that collapses are usually associated with high volume eruptive events.

The caveats of this method are that it relies on the assumption that the initial caldera was flat-topped with a height equal to the highest observable point at the present, overly simplifying its geometry. It also does not consider the infilling of the caldera depression by subsequent lavas and/or the modification of the rim shape by gradational processes. Thus, it simply provides an estimate for the volume of flows necessary to accommodate the observed collapse.

5.3. Eastern arcuate fracture system

Our mapping allows us to infer that some of the flows were fed from underlying dykes (Grosfils and Head, 1994; Parfitt and Head, 1993), given that they originate on the flanks and not at the summit. Such flow units erupted throughout the volcano's visible history and are associated with source groups a, b, c, d, e, f, g, and h (Fig. 8b). This is consistent with terrestrial mafic shield volcanoes, where flank eruptions can commonly predate the development of calderas (Simkin and Howard, 1970; Lockwood and Lipman, 1987), or be directly related to it (e.g., Kilauea lower rift zone eruption in 2018; Neal et al., 2018). Of particular interest are flows associated with the eastern arcuate fracture system (sAF-2) on Atira Mons' eastern flank (Fig. 25).

The eastern arcuate fracture system has a maximum diameter of ~350 km and fractures that are from a few kilometres to ~150 km in length. Its relationship with the flow units is ambiguous and difficult to assess. Most flow units do not seem to be affected by the existence of the arcuate fractures, implying the flows are being cut by the fractures, thus being older features. On the other hand, some flows appear to originate from these fractures (e.g., fEb-2, fEb-4, fEc-5, fEc-6), with some associated with the early stages of Atira Mons' exposed history, while others are among the youngest features (Fig. 20; see Section 5.1). This suggests the existence of multiple generations of these arcuate fractures, which periodically served as locations for magma accumulation and eruption and could be faults reactivated over time (e.g., Moore and Kokelaar, 1997). Such early existence of the arcuate fractures also opens the possibility of them documenting early collapse events of Atira Mons, that were subsequently overprinted by later flows. In this case, the observed summit would be contained inside the early and larger arcuate fractures, forming a nested structure, such as seen in different scales on Sacajawea Caldera (Head et al., 1992), Sapas Mons (Keddie and Head,

Fig. 25. Map fragment showing geologic units presumed to be sourced from the eastern arcuate fracture system sAF-2 (fEc-5, fEc-6, fEb-2, fEb-4). Green line marks Atira Mons' outer boundary.

1994), Derceto Corona (MacLellan et al., 2021) or Maat Mons (Mouginis-Mark, 2016). If that is the case, using the eastern arcuate fracture system's maximum diameter as a proxy for the size of the magma reservoir would yield an even larger value than the one suggested by the summit caldera's dimensions (116 km × 139 km).

The age of the youngest flank-fed flows (fEb-4, fEc-6) coincides with the age of the young summit flows (fSmt-2, fSmt-3). As noted previously, fSmt-3 shows signs of down-sagging after being emplaced. A possible explanation linking the later events on the summit to the eruptions on the eastern flank is the lateral injection of magma through dykes, which has been observed on the Bárdarbunga volcano, Iceland (Gundmundsson et al., 2016) and was suggested as an analogue for the Derceto large igneous province on Astkhik Planum (MacLellan et al., 2021).

5.4. Flexural moats

Considering the size of Atira Mons and the similarities between Venusian and terrestrial volcanic landforms (Herrick et al., 2005), a flexural moat (i.e., an annular topographic depression) might be expected on Venusian volcanoes similar to that associated with Hawaiian volcanoes (Watts and ten Brink, 1989). McGovern and Solomon (1998), McGovern et al. (2013, 2014, 2015), Galgana et al. (2013) and Herrick et al. (2005) have shown how in some cases, loading of the lithosphere by growing volcanoes on Venus can lead to the production of flexural topographic moats, as often demonstrated by both annular topographic depressions surrounding the base of the volcano, and the diversion of the termini of later-stage flows from the volcano, into the surrounding topographic depression. Although we specifically searched in detail for evidence of such phenomena, we found little indication of such topography or flow diversion and redirection into a flexural moat, associated with the observed flow apron and edifice. If such features do exist below Atira Mons, as seen at some other large volcanoes, than they must be below and interior to the base of the edifice (McGovern and Solomon, 1997) and perhaps detectable in the future using higher resolution gravity data. Currently observed changes in flow direction at the most distal parts of the flow units appear to be due to regional topography, slope changes, and barriers of preexisting structural features.

5.5. Comparison with terrestrial LIPs

Due to a lack of plate tectonics on Venus, Atira Mons, like all volcanoes on the planet, was emplaced in an intraplate setting. Here we estimate the volume of flows associated with the volcano and the size of the associated arcuate fracture system (Fig. 3a; Ernst et al., 2003; Section 5.3, this manuscript) to determine whether Atira Mons should be considered analogous to a terrestrial LIP.

5.5.1. Estimation of volume and size of the associated arcuate fracture system

As noted above, the areal extent of the volcanism of Atira Mons is ~300,000 km^2. The volume of the volcano is estimated in two ways (details in Appendix A) and the results are summarized here. One calculation (V_T) estimates the volume of volcano above a flat reference plane, with this plane coinciding with the lowest elevation inside the perimeter of the volcano. The problem with this approach is that the underlying regional topography is added to the calculation. To address this, we attempt to estimate the surface of the underlying regional topography with Voronoi polygons (Yamada, 2016) and then subtracted this from V_T to obtain V_E, the volume of the volcano. Therefore:

$$V_T = 271,339.7 \text{ km}^3$$

$$V_E = 47,152.6 \text{ km}^3$$

It is worth noting that both these estimates assume that no loading and flexure has occurred, since no flexural moat was observed (see
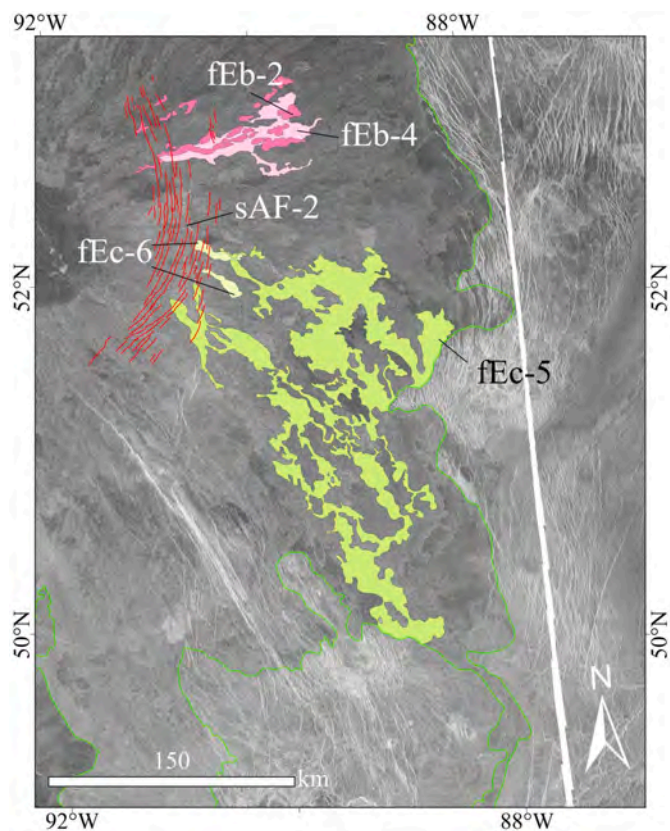
Section 5.4). However, the topographic signature of terrestrial flexural moats can be erased by filling or overfilling of moat depressions with volcanic materials (e.g., Filmer et al., 1993, 1994). Thus, the real volumes of this and other Venusian volcanoes would be much larger than the volume of their visible central edifices (7–12 times larger as suggested by McGovern and Solomon, 1997). Therefore, our estimates likely represent minimum volumes, since the moat fill and intrusions associated with Atira Mons are not accounted for, and more accurate values may be devised when higher resolution gravity datasets become available.

Terrestrial LIPs are defined on the basis of three characteristics: intraplate setting or characteristics, large volume ($\geq$100,000 km^3, or $\geq$100,000 km^2, if using the areal extent as a proxy), and short duration of emplacement ($<$5 myr, or multiple short duration pulse spanning up to a few 10s of myr) (Ernst, 2014, 2021). As mentioned in the introduction, volcanism on Venus is attributed to intraplate magmatism (Head et al., 1992; Ernst and Desnoyers, 2004; Solomatov and Moresi, 1996; Stern et al., 2018). In terms of areal extent, Atira Mons also fits this definition, having about three times the minimum size of a terrestrial LIP. Considering its volume, the larger estimate ($\sim$270,000 km^3) is of the same order as the Columbia River flood basalt province ($\sim$210,000 km^3, e.g., Reidel and Hooper, 1989). However, assessing the exact duration of such events on Venus is not possible now since there is no geochronologic data for Atira Mons. Nevertheless, what we can say is that all visible units are collectively associated with a single volcanic center, thus with a single event. Therefore, the six visible stages of Atira Mons history could be considered analogous to multiple formations erupted in terrestrial LIPs (e.g. Deccan LIP; see general characteristics and references in Ernst et al., 2014), which can be emplaced over the course of a few myr to 10s of myr.

Additionally, we must consider the intrusive component associated with a volcanic center. The only intrusive component that we can easily measure with the current datasets is the dyke swarm, here expressed as the system of arcuate fractures on the eastern flank (sAF-2), with maximum diameter $\sim$350 km and maximum length $\sim$150 km. These are comparable to terrestrial circumferential dyke swarms, that have diameters $\sim$450 km to $\sim$2500 km (Buchan and Ernst, 2018).

Furthermore, a previous study (Ernst et al., 2003) identified a large radiating graben system (interpreted to overlie a dyke swarm) fanning outward from the southern side of Atira Mons (Fig. 3a), extending up to about 1200 km from the center of the volcano. The age relationship of the distant radiating graben to Atira Mons' flows is not clear due to the lack of any clear interaction between the structures and the flows. Furthermore, the fact that this system is not radiating in all directions causes its genetic association with Atira Mons to be more ambiguous. However, these grabens are crosscutting the regional plains (Fig. 3a and c), which are partially overlain by Atira Mons' flows. This supports the hypothesis of them forming as a result of an initial mantle plume ascent phase with radial dyke emplacement (Grosfils and Head, 1994; Ernst et al., 2001) on the regional plains. The lack of radial graben on the volcano itself is possibly related to Atira Mons' shallow magma reservoir, which precludes the development of such features on the upper lithosphere, as suggested by modelling (Galgana et al., 2011). Moreover, the volume of the underlying dyke swarm component is difficult to quantify, but the presence of such a large radiating swarm is indicative of a buffered magma supply (Parfitt and Head, 1993; Wilson and Head, 2002), and thus further indicates the presence of a large mantle plume, a phenomenon typically linked with LIPs (Ernst et al., 2001). In summary, Atira Mons resembles terrestrial LIPs in several ways.

5.5.2. Terrestrial analogue: Apolaki Caldera of the Benham Rise Oceanic LIP

With Atira Mons being interpreted as a large resurgent mafic caldera, it is difficult to find an Earth analog with similar scale, characteristics and related to a LIP, since most large resurgent calderas are associated with silicic volcanoes (e.g., Lipman, 2000; Trasatti et al., 2019).
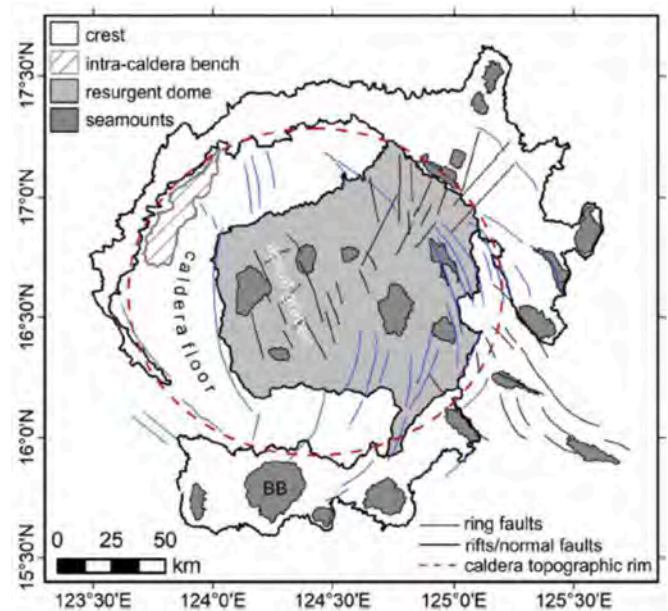

Fig. 26. Morphological features of Apolaki Caldera. BB = Benham Bank. After Barretto et al., 2020.

However, the Apolaki Caldera (Fig. 26) on the Benham Rise Oceanic LIP, as described by Barretto et al. (2020) shares many characteristics with Atira Mons and is a potential terrestrial analog.

The Benham Rise LIP covers an area of $\sim$110,000 km^2, about one third of the area covered by Atira Mons, and is located in the western portion of the Philippine Sea. Crustal thickness in the Benham Rise area is $\sim$15 km and falls within the range of the crustal thickness that was modeled by Jiménez-Diaz et al. (2015) for the Atira Mons region. The Benham Rise is characterized by a platform base ($\sim$310 km x $\sim$330 km) that resembles shield volcanoes with its shallow slopes (less than $\sim$1° to $\sim$3°), and its main body crest, which has steeper slopes between $\sim$4° and $\sim$8°. Generally, the volcano rises from a depth of $\sim$5200 m up to 2500 m, with the guyot (Benham Bank) reaching $\sim$50 m below sea level. Atira Mons also shows a similar morphology, with flanks having shallower slopes (less than a degree in average), in comparison with the summit region (maximum of $\sim$7.5°).

A striking similarity between these two volcanic centers is the presence of a large central caldera. The Apolaki Caldera has a diameter of $\sim$150 km, while the Atira Mons' caldera varies from $\sim$115.8 to 138.5 km, suggesting large magma reservoirs for both volcanic centers. Furthermore, both summit regions are characterized by incomplete near-circular rims that partially bound a central depression, and that were breached by syn- or post-collapse eruptive events. This breaching is speculated to be caused by an explosive eruption in Apolaki. Interpreting the same origin for the caldera collapse and subsequent breaching of Atira Mons' eastern rim is controversial since mapping did not reveal any pyroclastic deposits. Furthermore, evidence for pyroclastic deposits is scarce on Venus (e.g., Ghail and Wilson, 2013), due to high atmospheric pressure and lack of water, which are thought to inhibit explosive volcanism (e.g., Head and Wilson, 1986).

The Apolaki Caldera also preserves evidence of late-stage mafic resurgence, similar to what is interpreted to have occurred on Atira Mons, due to the presence of two smaller shield volcanoes on its summit. However, in the Apolaki Caldera, resurgence is expressed very differently, with a resurgent dome producing a $\sim$1.5 km uplift on the caldera's floor and the emplacement of a series of seamounts (Fig. 26).

That said, some important differences between these two volcanic centers should be considered. Firstly, while both are linked to intraplate magmatism, Benham Rise formed by the interaction of a hotspot and an oceanic spreading center. Secondly, ground-truthing data shows that

some of the Rise's late-stage seamounts are more silicic (e.g., Vinogra-dov Seamount), something that is impossible to assess for Atira Mons on Venus with the Magellan dataset. Lastly, the Rise contains volcanic constructs thought to be associated with rift zones and triple junctions (e.g., Molave Spur), features that have not been identified for Atira Mons.

5.6. Lessons for future detailed mapping of flows

Detailed geological mapping of Atira Mons highlighted a series of limitations of the Magellan dataset. During our work the main challenges of our approach include how to:

- Discern lava breakouts from isolated patches of older flows (Fig. 27a).
- Determine if narrow channels superimposed on a flow are part of the flow or represent younger pulses that crosscut an older unit (Fig. 27b).
- Assess whether flow units of similar morphology and brightness belong to the same geologic unit.
- Determine whether downslope radar backscatter changes indicate separate flows or variations in roughness of a single flow (Fig. 27c).
- Recognize and interpret diffuse boundaries between flows.
- Avoid overinterpretation of subtle features since we mapped close to the resolution limit of the datasets.
- Consider Magellan's coarse altimetry dataset (10–30 km footprint; 80–100 m vertical resolution).

Interpretations that appear more likely from a geologic perspective were preferred, while objects with an unknown or ambiguous origin were separately defined and excluded from the suggested geological

history. Much of these issues will potentially be solved by the multiple spacecraft heading to Venus in the coming decades, namely VERITAS (Smrekar et al., 2022), EnVision (Ghail et al., 2020), DAVINCI+ (Glaze et al., 2017), Venera-D (Zasova et al., 2019), VOICE (Wang et al.) and Shukrayaan-1 (Sundararajan, 2021).

6. Conclusions

Detailed geologic mapping on a scale of 1:500,000 has revealed that Atira Mons is a large shield volcano containing a multiple-event, resurgent, asymmetric and elliptical basaltic caldera (116 km × 139 km) on top of a shallow magma reservoir. Caldera morphology suggests that collapse may have involved trapdoor-like and down-sagging episodes, with possible periodic lateral emplacement of low-volume lavas through an arcuate fracture system ~350 km in diameter on the volcano's eastern flank. Alternatively, Atira Mons' summit morphology could be related to the development and breaching of a giant lava lake. Furthermore, the presence of a distal radiating graben system suggests an initial plume head ascent phase with lateral dyke emplacement.

Flow mapping revealed tens of sources, with most of them being associated with the summit or near-summit region, indicating that magma moved predominantly through conduits overlying the magma reservoir. However, other flows were interpreted to be sourced from fissures and/or vents on Atira Mons' flanks.

Analysis of cross-cutting relationships between geologic units indicates that the most voluminous flows pertain to Atira Mons' early episodes of volcanic activity, with younger flows being associated with smaller eruptions. Aside from the summit region, which experienced caldera formation, the topography of the region did not change significantly after the emplacement of flows, as evidenced by most flow units having their trends controlled by the older regional topography.
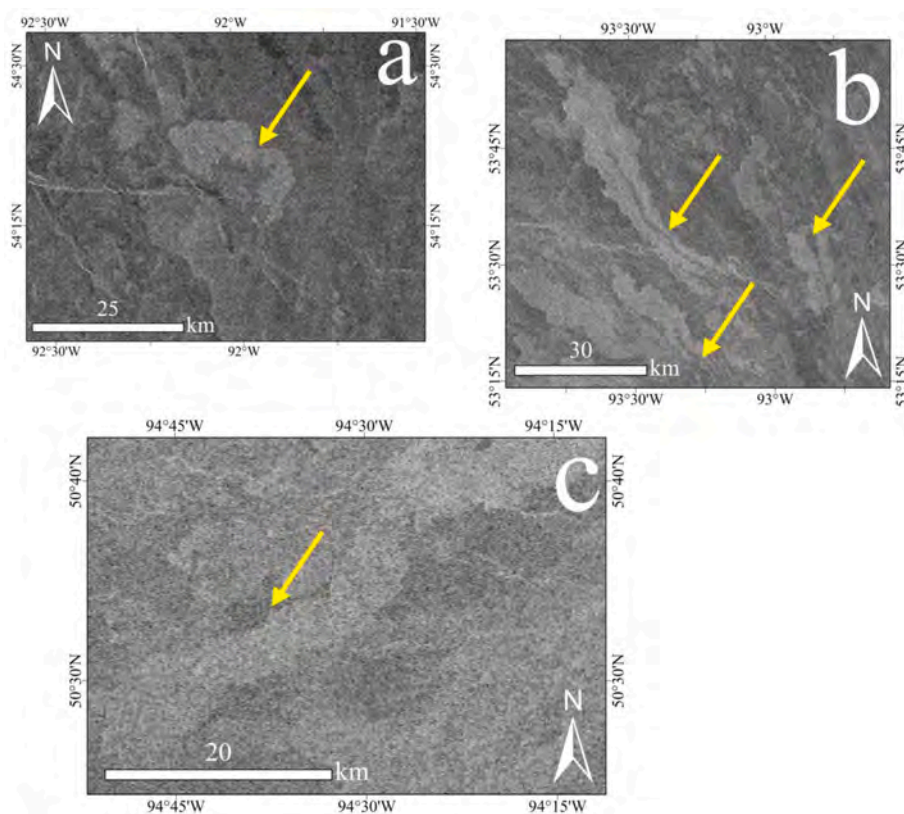
Fig. 27. Some of the ambiguities presented by analyzing Magellan's SAR images (yellow arrows point to discussed features): a) Radar-bright lava breakouts or isolated patches of older flows? b) Younger radar-dark channels cross-cutting older radar-bright flows or feeder channels for these flows? c) Do the downslope (NE to SW) changes in radar brightness represent natural variations in a single flow or a different geologic unit altogether.?.

Atira Mons' areal extent (~300,000 km^2), volume estimates (~47,000 to 270,000 km^3), intraplate setting, evidence of radial and arcuate systems similar to terrestrial dyke swarms, association of all flow units with a single event, as well as its similarities with Earth's largest mafic caldera, Apolaki Caldera on the Benham Rise LIP, favor the classification of Atira Mons as a Venusian LIP.

The process of geologic mapping revealed several obstacles to producing a more complete geological interpretation using the current dataset. These problems will potentially be solved by the new missions that will be sent to Venus over the next decades, helping to better constrain and refine geologic interpretations regarding the evolution of the planet.

CRediT authorship contribution statement

C.H.G. Braga: Conceptualization, Methodology, Visualization, Writing – original draft, Writing – review & editing. **E.G. Antropova:** Writing – original draft, Writing – review & editing. **R.E. Ernst:** Conceptualization, Funding acquisition, Supervision, Writing – original draft, Writing – review & editing. **H. El Bilali:** Conceptualization, Supervision, Writing – original draft, Writing – review & editing. **J.W. Head:** Writing – review & editing. **K.L. Buchan:** Writing – review & editing.

Declaration of competing interest

The authors declare the following financial interests/personal

Data availability

Data will be made available on request.

Acknowledgements

Appendix A. Volume Estimates of Atira Mons

In previous studies, authors estimated the thickness of lava flows based on the average height differences between flows (e.g., MacLellan et al., 2021). Here we choose a different approach. As part of the lobate plains (pl in Ivanov and Head, 2011), Atira Mons' geologic units are the youngest globally widespread geologic units in our study area. This was further confirmed by our mapping. Therefore, the area of the units related to it represents a true exposure. Using this information together with topographic data, we suggest a method for estimating minimum volume of eruptions over this volcano's visible eruption history.

The method consists of calculating the total volume V_T of the volcano(Fig. A1a) above a reference plane (Fig. A1b) using the "Venus Magellan Global Topography 4641m v2" dataset (downloaded at www.astrogeology.usgs.gov) and the "Surface Volume" tool from the 3D Analyst extension in ArcPro. This is done by extracting the area corresponding to Atira Mons and using this fragment of the surface to calculate the total volume. Using this approach gives an overestimate, thus a maximum volume (V_T), since part of the underlying relief is possibly included in the calculation (Fig. A1b). To better constrain the volume, one can estimate the elevation underneath the volcano (Fig. A1c), calculate the volume of the regional relief without the volcano (V_R) and then subtract V_T from V_R to obtain V_E, the volume of the volcano.

To accomplish this, we chose to use Voronoi polygons (Yamada, 2016). They provide a rough estimate, but preferable in comparison with interpolation methods, such as Inverse Distance Weighted or Kriging, since the latter are used when sampling is denser and even (Babish, 2000). In our case, the elevation estimate is carried out between areas that are sometimes hundreds of kilometers away from each other and the elevation values are unevenly distributed in space.
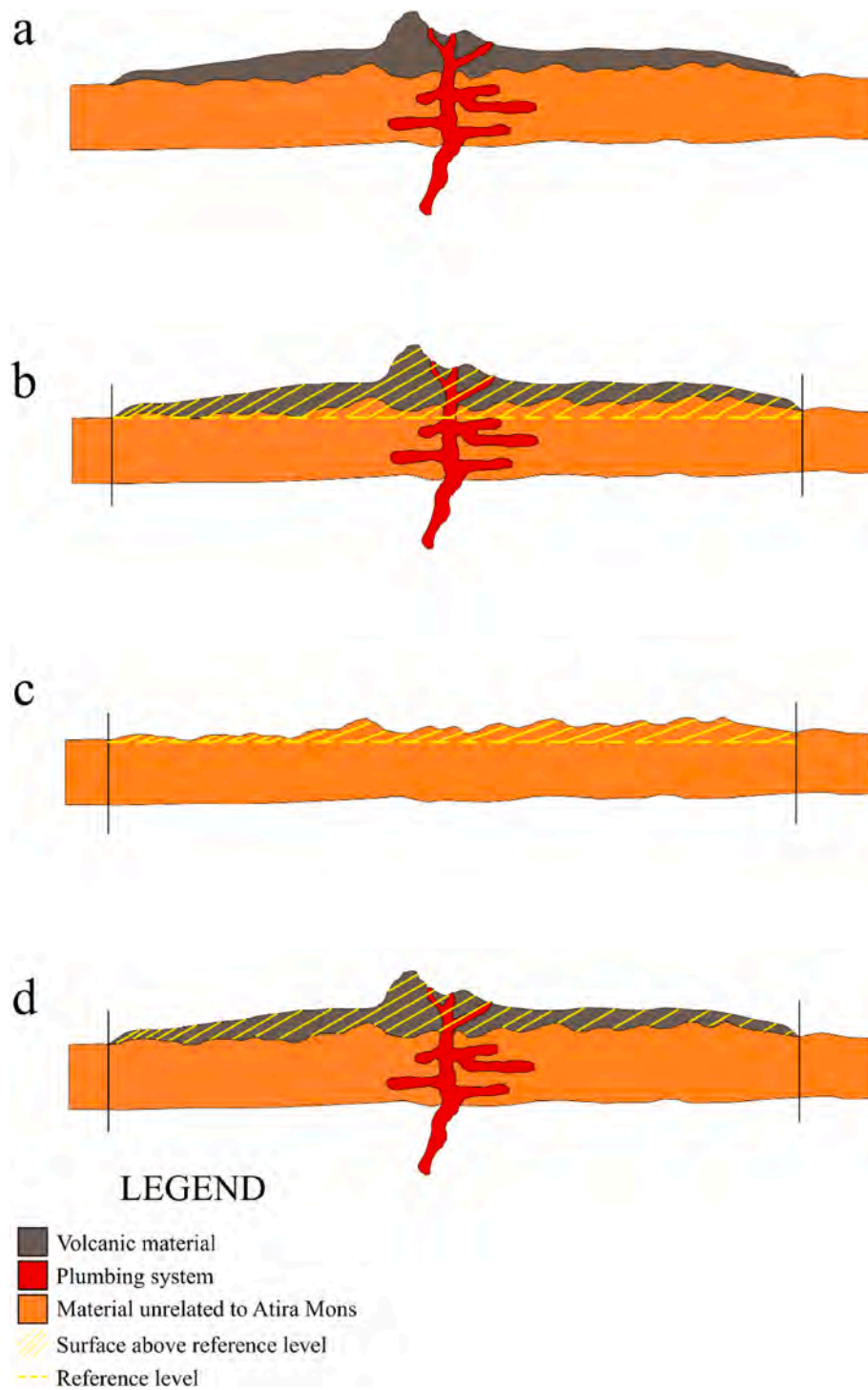
Fig. A1. Schema describing the estimates used to constrain Atira Mons' volume. a) cross section of the volcano; b) Total volume (V_T) estimated from a reference level; c) Volume of the estimated regional topography (V_R) underneath the volcano from a reference level; d) Volume of the volcano (V_E) calculated by subtracting V_R from V_T.
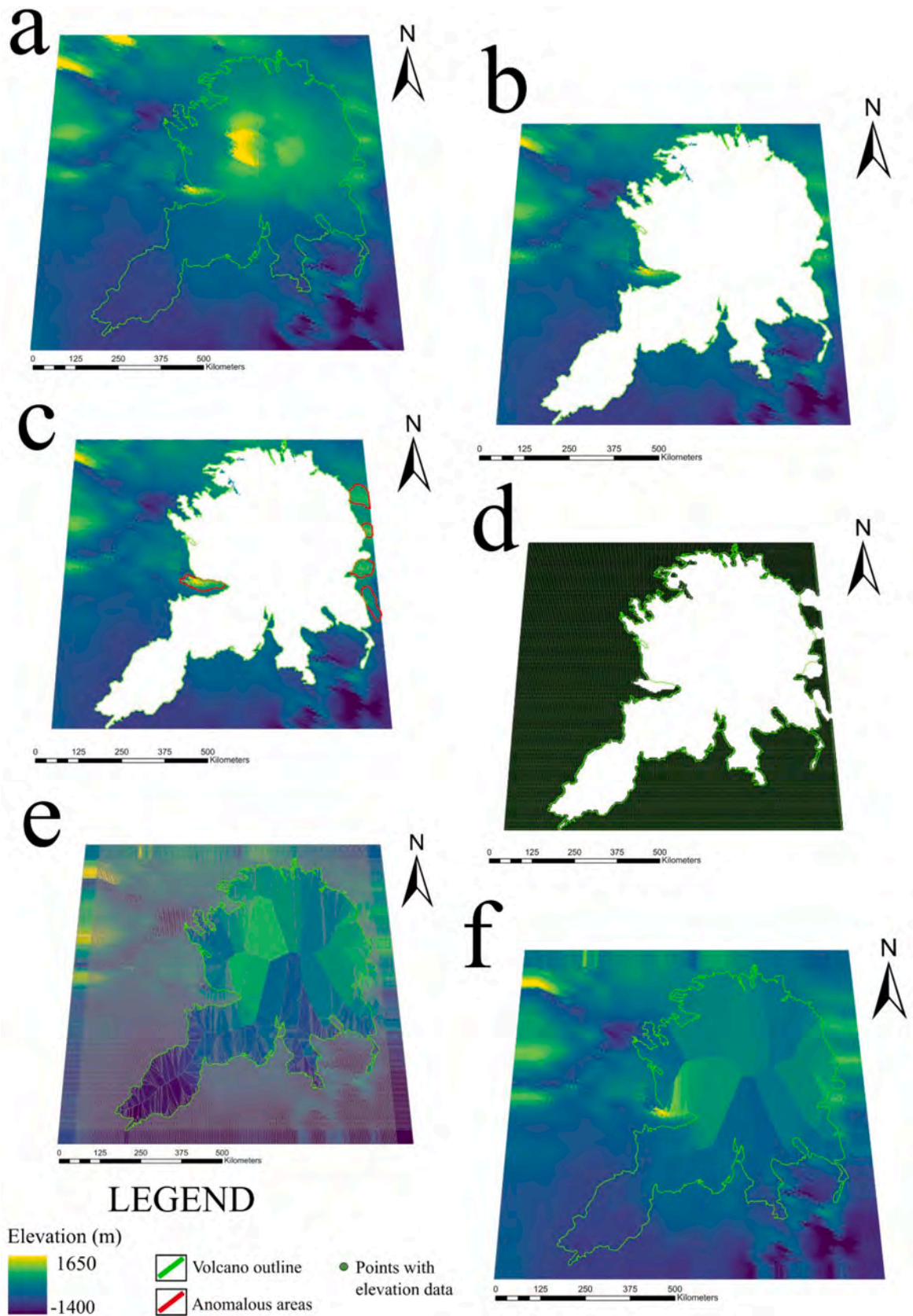
Fig. A2. Steps for estimating the regional topography underneath Atira Mons (green line). a) Global topography; b) Global topography without Atira Mons; c) Anomalous elevations marked for removal (red lines); d) Point dataset representing global topography without Atira Mons; e) Voronoi polygons generated from (d); f) Voronoi polygons converted to a raster. Volcano centered on 51.4°N, 272.9°E (92.9°W).

The first step is to remove Atira Mons' influence on the topography (Fig. A2a). This is done by deleting pixels of the altimetry dataset that are located inside the volcano's perimeter with the tool "Extract by Mask". The mask corresponds to the volcano's boundaries, while the extraction area

corresponds to the area outside of the polygon. As a result, the new raster contains the topographic data of the region without the volcano (Fig. A2b). The next step is to delete anomalous topographic highs and lows (groove belts, for instance) to avoid boundary effects when estimating the elevation underneath Atira Mons. This is done manually by mapping these areas as polygons and then excluding the pixels located inside them (Fig. A2c). After that, the further modified raster is converted to points, so the Voronoi polygons can be generated (Fig. A2d). Using the built-in instrument to create these polygons yields a vector file (Fig. A2e). To use this data on the "Surface Volume" tool, the polygons are converted to a raster. This new raster contains the estimated elevation values by Voronoi polygons and the altimetry data outside Atira Mons and the topographic anomalies (Fig. A2f). From this file, the area inside Atira Mons' outer boundary is extracted, which yields a raster with the estimated regional elevations under the volcano. Then, the "Surface Volume" tool is applied to this raster and V_R is obtained. As mentioned before, subtracting V_R from V_T yields V_E.

The caveats of this approach are:

- Assuming a flat boundary under the volcano for calculating V_T.
- Discarding the effects of flexure on the lithosphere and the presence of fill and overfill material on moat depression surrounding large volcanoes (e. g., McGovern and Solomon, 1997).

Therefore, such estimates (V_T and V_E) provide minimum volumes for Atira Mons' volcanism.

Appendix B. Characteristics of Atira Mons' Geologic Units

Table B1

Characterization of Atira Mons' geologic units. f – lava flows (flucti); g – gradational units; sh – shield volcanoes; rgd – deformed ridge; u – units of unknown origin.

Unit	Exposed area (km^2)	Source Group	Present source elevation (m above MPR)	Maximum Slope (deg)	Mean radar backscatter (0–255)	Maximum flow length (km)	Flow stage
Summit units (Smt)							
fSmt-1	1886.8	l	800–850	5.11	108.686	50	4
fSmt-2	3170.6	l	800–850	4.16	95.976	60	6
fSmt-3	4865.4	l	800–850	1.61	91.472	70	6
shSmt-1	472.0	l	800–850	1.06	96.0422	10–15	6
gSmt-1	698.0	–	–	3.86	107.407	–	5
uSmt-1	35.2	–	–	0.31	114.206	–	–
Southwestern units (SW)							
fSWa-1	2769.2	k	800–850	2.43	105.671	100	3b
fSWa-2	1569.8	k	800–850	4.79	107.023	70	3b
fSWa-3	79.8	k	800–850	0.33	101.781	35	3b
fSWb-1	3925.7	a	150	0.31	114.551	230	1
fSWb-2	28811.7	k, l	600	0.66	108.625	580	1
fSWb-3	4348.8	a	150	0.34	111.325	230	1
fSWb-4	8247.9	a	150	0.44	108.453	385	1
fSWb-5	23594.0	k, l	600	0.37	104.603	510	1
uSWb-1	281.1	–	–	0.30	60.368	–	–
fSWc-1	3532.0	k	800–850	3.62	115.79	390	1
fSWc-2	2161.6	k	800–850	0.95	112.74	300	1
fSWc-3	4607.0	k	800–850	1.99	111.204	320	1
fSWc-4	8742.5	c	400–450	0.53	112.677	300	3a
fSWc-5	4004.8	k	800–850	0.65	110.188	150	3b
fSWc-6	3563.2	b	600	0.53	113.146	145	3b
fSWc-7	16266.4	k	800–850	3.54	104.707	261	4
fSWc-8	600.8	k	800–850	4.49	96.897	12	5
Western units (W)							
fW-1	3026.2	–	–	2.53	107.992	200	3a
Northern units (N)							
fNa-1	1086.3	h	450–500	0.25	85.207	70	2b
fNa-2	2824.3	l	850–900	0.60	101.043	185	2b
fNa-3	1670.8	i	900–950	0.61	99.882	150	2b
fNa-4	2703.3	f	500–550	0.97	91.814	100	2b
fNa-5	29618.6	l	900–1100	2.67	92.709	230	3a
fNa-6	3050.2	j	700–1000	1.53	97.9132	160	3b
fNa-7	4320.5	i	900–950	3.92	104.179	140	3b
fNa-8	11203.9	j	700–1000	1.93	94.791	200	3b
fNa-9	4223.3	i	900–950	4.15	97.685	130	5
fNb-1	526.5	g	300–350	0.36	92.210	45–220	3b
fNb-2	698.9	n	500–600	0.74	104.405	35	3b
fNb-3	2585.6	m	650–700	0.41	99.565	210	3b
fNb-4	415.3	n	450–500	0.22	93.133	75	3b
fNb-5	9217.2	n	700–800	0.87	96.564	215	5
fNb-6	9059.5	l	800–1050	1.73	91.116	210	6
uNb-1	218.7	–	–	0.37	106.427	–	–
uNb-2	522.0	–	–	0.25	97.100	–	–
shNb-1	–	–	–	–	–	–	–
Eastern units (E)							
fEa-1	6660.1	l	800–850	1.19	104.245	220	1
fEa-2	3484.4	l	800–850	0.71	110.181	270	2a

Table B1 (*continued*)

Unit	Exposed area (km²)	Source Group	Present source elevation (m above MPR)	Maximum Slope (deg)	Mean radar backscatter (0–255)	Maximum flow length (km)	Flow stage
rdgEa-1	5283.5	–	–	2.1	116.221	–	1
uEa-1	396.5	–	–	0.54	120.494	–	–
fEb-1	4917.9	–	–	1.23	96.526	260	2a
fEb-2	818.1	p	700–750	0.71	110.181	110	2a
fEb-3	37561.17	l	750–800	1.05	104.395	250	2a
fEb-4	1037.1	p	700–750	0.46	97.625	100	6
fEb-5	380.4	d	500–600	0.37	100.054	65	6
fEc-1	957.8	–	–	1.45	110.762	330	2a
fEc-2	3158.7	–	–	0.42	106.765	415	2a
fEc-3	726.8	–	–	0.86	102.523	270	2a
fEc-4	3831.5	–	–	1.31	105.679	305	2a
fEc-5	9618.8	e	750–800	0.94	100,720	270	3b
fEc-6	252.2	e	750–850	0.49	111.386	30	6
fEd-1	321.6	o	800–850	0.63	109.513	60	4
fEd-2	2254.6	o, l	800–850	2.31	104.604	90	6
fEd-3	2522.6	n	800–850	0.80	100.391	200	6

Table B2
Characterization of sources associated with Atira Mons

Source Nº	Source Group	Latitude (N)	Longitude (W)	Location	Present source elevation (m above MPR)	Type
1	a	49.5284	94.6845	Flank	150	Inferred vent
2	b	51.0239	93.5043	Flank	600	Inferred vent
3	c	50.7593	92.5276	Flank	400	Inferred vent
4	d	51.0171	90.5884	Flank	500	Inferred fissure
5	d	51.1840	90.5065	Flank	550	Inferred vent
6	d	51.2516	90.4818	Flank	550	Inferred vent
7	e	52.2792	90.4871	Flank	850	Inferred fissure
8	e	52.1018	90.5712	Flank	750	Inferred fissure
9	e	51.9282	90.8927	Flank	750	Inferred fissure
10	e	52.0223	90.6675	Flank	750	Inferred fissure
11	e	52.2239	90.3945	Flank	750	Inferred fissure
12	f	53.1914	89.8869	Flank	500	Inferred vent
13	g	53.9449	90.0283	Flank	350	Inferred vent
14	h	53.8581	91.0053	Flank	450	Inferred vent
15	h	54.0482	91.2240	Flank	450	Inferred vent
16	i	52.9446	92.8363	Near-summit	900	Inferred vent
17	j	52.4841	93.6011	Near-summit	950	Inferred vent
18	k	51.8384	93.3441	Near-summit	850	Inferred vent
19	k	51.7395	92.7716	Near-summit	800	Inferred vent
20	l	52.2936	92.8905	Summit	1100	Confirmed vent
21	l	52.3538	92.7311	Summit	900	Confirmed vent
22	l	52.3546	92.6347	Summit	950	Confirmed vent
23	l	52.2733	92.5740	Summit	900	Confirmed vent
24	l	52.2726	92.5465	Summit	850	Confirmed vent
25	l	52.2565	92.6888	Summit	950	Confirmed vent
26	l	52.2741	92.1249	Summit	650	Confirmed vent
27	l	52.5897	92.5122	Summit	850	Confirmed vent
28	l	52.0738	92.4647	Summit	850	Confirmed vent
29	l	51.9989	92.3698	Summit	800	Confirmed vent
30	l	52.7605	92.4371	Summit	850	Inferred vent
31	l	52.3311	92.6418	Summit	900	Confirmed vent
32	l	52.3052	92.6206	Summit	900	Confirmed vent
33	l	52.1628	92.6426	Summit	950	Confirmed vent
34	l	52.3180	92.7513	Summit	1000	Confirmed vent
35	l	52.3107	92.6733	Summit	950	Confirmed vent
36	l	52.5643	92.5129	Summit	850	Confirmed vent
37	l	52.2673	92.8972	Summit	1100	Confirmed vent
38	l	52.3043	92.7991	Summit	1050	Confirmed vent
39	m	52.7768	92.0223	Near-summit	600	Confirmed vent
40	m	52.7435	91.5593	Near-summit	700	Confirmed vent
41	m	52.9752	91.8810	Near-summit	700	Inferred vent
42	n	52.4532	91.7901	Summit	750	Confirmed vent
43	n	52.4858	91.7318	Summit	700	Confirmed vent
44	n	52.4919	91.6567	Summit	700	Confirmed vent
45	n	52.4416	91.7095	Summit	750	Confirmed vent
46	n	52.2761	91.5045	Near-summit	850	Inferred vent
47	o	51.9995	91.6591	Near-summit	800	Inferred vent
48	p	52.7438	90.9269	Near-summit	700	Inferred fissure

Appendix C Supplementary data

Supplementary data to this article can be found online at https://doi.org/10.1016/j.pss.2024.105879.

References

Acocella, V., Funiciello, R., 1999. The interaction between regional and local tectonics during resurgent doming: the case of the island of Ischia, Italy. J. Volcanol. Geoth. Res. 88 (1–2), 109–123. https://doi.org/10.1016/S0377-0273(98)00109-7.

Antropova, E.G., Braga, C.H.G., Ernst, R.E., El Bilali, H., Head, J.W., Ivanov, B.A., 2023. Characterization of a 2700 km long bolide airburst chain, Phoebe Regio, Venus. Planet. Space Sci. 228, 105636 https://doi.org/10.1016/j.pss.2023.105636.

Babish, G., 2000. Geostatistics without Tears: A Practical Guide to Geostatistics, Variograms and Kriging. Environment Canada.

Barretto, J., Wood, R., Milsom, J., 2020. Benham rise unveiled: morphology and structure of an Eocene large igneous province in the west Philippine basin. Mar. Geol. 419, 106052 https://doi.org/10.1016/j.margeo.2019.106052.

Barsukov, V.L., et al., 1986. The geology and geomorphology of the Venus surface as revealed by the radar images obtained by Veneras 15 and 16. Proc.16th Lunar and Planetary Sci. Conf. 91 (B4), 378–398. https://doi.org/10.1029/JB091iB04p0D378.

Barsukov, V.L., 1992. Venusian igneous rocks. In: Barsukov, V.L., et al. (Eds.), Venus Geology, Geochemistry, and Geophysics (Research Results from the USSR). University of Arizona Press, pp. 165–176.

Basilevsky, A.T., Burba, G.A., Ivanov, M.A., Bobina, N.N., Shashkina, V.P., Head, J.W., 1999. Photogeologic Map of Northern Venus: a Progress Report, 30th Lunar and Planetary Science Conference. Abstract #1295.

Basilevsky, A.T., Head, J.W., 2000. Rifts and large volcanoes on Venus: global assessment of their age relations with regional plains. J. Geophys. Res.: Planets 105 (E10), 24583–24611. https://doi.org/10.1029/2000JE001260.

Basilevsky, A.T., Head, J.W., 2003. The surface of Venus. Rep. Prog. Phys. 66 (10), 1699. https://doi.org/10.1088/0034-4885%2F66%2F10%2FR04, 173.

Basilevsky, A.T., Head, J.W., 2007. Beta Regio, Venus: evidence for uplift, rifting, and volcanism due to a mantle plume. Icarus 192, 167–187. https://doi.org/10.1016/j.icarus.2007.07.007.

Blake, S., Bruno, B.C., 2000. Modelling the emplacement of compound lava flows. Earth Planet Sci. Lett. 184 (1), 181–197. https://doi.org/10.1016/S0012-821X(00)00278-8.

Branney, M.J., 1995. Downsag and extension at calderas: new perspectives on collapse geometries from ice-melt, mining, and volcanic subsidence. Bull. Volcanol. 57, 303–318. https://doi.org/10.1007/BF00301290.

Buchan, K.L., Ernst, R.E., 2018. Giant circumferential dyke swarms: catalogue and characteristics. In: Srivastava, R.K., et al. (Eds.), Dyke Swarms of the World: A Modern Perspective. Springer Geology, pp. 1–44. https://doi.org/10.1007/978-981-13-1666-1.

Buchan, K.L., Ernst, R.E., 2021. Plumbing systems of large igneous provinces (LIPs) on Earth and Venus: investigating the role of giant circumferential and radiating dyke swarms, coronae and novae, and mid-crustal intrusive complexes. Gondwana Res. 100, 25–43. https://doi.org/10.1016/j.gr.2021.02.014.

Byrnes, J.M., Crown, D.A., 2002. Morphology, stratigraphy, and surface roughness properties of Venusian lava fields. J. Geophys. Res.: Planets 107 (E10), 9-1–9-122. https://doi.org/10.1029/2001JE001828.

Byrne, P.K., Ghail, R.C., Gilmore, M.S., Celâl Şengör, A.M., Klimczak, C., Senske, D.A., Whitten, J.L., Khawja, S., Ernst, R.E., Solomon, S.C., 2021. Venus tesserae feature layered, folded, and eroded rocks. Geology 49 (Nº 1), 81–85. https://doi.org/10.1130/G47940.1.

Campbell, B.A., Arvidson, R.R., Shepard, M.K., Brackett, R.A., 1997. Remote sensing of surface processes. In: Bougher, S.W., et al. (Eds.), Venus II: Geology, Geophysics, Atmosphere, and Solar Wind Environment. The University of Arizona Press, pp. 503–526. https://doi.org/10.2307/j.ctv27tct5m.26.

Christensen, P., Engle, E., Anwar, S., Dickenshield, S., Noss, D., Gorelick, N., Weiss-Malik, M., 2009. JMARS – A Planetary GIS. American Geophysical Union Fall Meeting. Abstract id. IN22A-06, 2009.

Clague, D., Moore, J., Reynolds, J., 2000. Formation of submarine flat-topped volcanic cones in Hawai'i. Bull. Volcanol. 62, 214–233. https://doi.org/10.1007/s004450000088.

Cole, J.W., Milner, D.M., Spinks, K.D., 2005. Calderas and caldera structures: a review. Earth Sci. Rev. 69 (1–2), 1–26. https://doi.org/10.1016/j.earscirev.2004.06.004.

Cousens, B.L., Clague, D.A., 2015. Shield to rejuvenated stage volcanism on Kauai and Niihau, Hawaiian islands. J. Petrol. 56 (8), 1547–1584. https://doi.org/10.1093/petrology/egv045.

Crumpler, L.S., Aubele, J.C., 2000. Volcanism on Venus. In: Sigurdsson, H., et al. (Eds.), Encyclopedia of Volcanoes. Academic Press, pp. 727–770.

Crumpler, L.S., Aubele, J.C., Senske, D.A., Keddie, S.T., Magee, K.P., Head, J.W., 1997. Volcanoes, and centers of volcanism on Venus. In: Bougher, S.W., et al. (Eds.), Venus II: Geology, Geophysics, Atmosphere, and Solar Wind Environment. University of Arizona Press, pp. 697–756. https://doi.org/10.2307/j.ctv27tct5m.26.

Dietterich, H., Diefenbach, A., Soule, A., Zoeller, M., Patrick, M., Major, J., Lundgren, P., 2021. Lava effusion rate evolution and erupted volume during the 2018 Kilauea lower East Rift Zone eruption. Bull. Volcanol. 83 https://doi.org/10.1007/s00445-021-01443-6.

Dohm, J.M., Tanaka, K.L., Skinner, J.A., 2011. Geologic Map of the Metis Mons Quadrangle (V-6), Venus, vol. 3158. U. S. Geological Survey Scientific Investigations, Map.

El Bilali, H., Ernst, R.E., Buchan, K.L., 2022. Maat Mons, Atla Regio, Venus. Magmatic and Tectonic History from Detailed Mapping, 52nd Lunar And Planetary Science Conference. Abstract #2548.

Ernst, R.E., 2001. Giant dike swarms: Earth, Venus and Mars. Annu. Rev. Earth Planet Sci. 29, 489–534. https://doi.org/10.1146/annurev.earth.29.1.489.

Ernst, R.E., 2014. Large Igneous Provinces. Cambridge University Press, p. 666.

Ernst, R.E., 2021. Large igneous provinces. In: Alderton, D., Elias, S.A. (Eds.), Encyclopaedia of Geology, , second ed.vol. 2. Academic Press, pp. 60–68.

Ernst, R.E., Desnoyers, D.W., Head, J.W., Grosfils, E.B., 2003. Graben–fissure systems in Guinevere Planitia and Beta Regio (264°–312°E, 24°–60°N), Venus, and implications for regional stratigraphy and mantle plumes. Icarus 164 (2), 282–316. https://doi.org/10.1016/S0019-1035(03)00126-X.

Ernst, R.E., Desnoyers, D.W., 2004. Lessons from Venus for understanding mantle plumes on Earth. Phys. Earth Planet. In. 146 (Issues 1–2), 195–229. https://doi.org/10.1016/j.pepi.2003.10.012.

Ernst, R.E., El Bilali, H., Head, J.W., 2022. International Venus Research Group (IVRG): Detailed mapping to develop geological histories of 40+ area of Venus. Annual Meeting of Planetary Geologic Mappers, June 22–23, 2022. Arizona/Virtual, Flagstaff.

Filmer, P.E., McNutt, M.K., Wolfe, C.J., 1993. Elastic thickness of the lithosphere in the marquesas and society islands. J. Geophys. Res. 98 (B11), 19565–19577. https://doi.org/10.1029/93JB01720.

Ford, J.P., Plaut, J.J., Weitz, C.M., Farr, T.G., Senske, D.A., Stofan, E.R., Michaels, G., Parker, T.J., 1993. Guide to Magellan Image Interpretation, vols. 93–24. Jet Propulsion Laboratory Publication, p. 123.

Filmer, P.E., McNutt, M.K., Webb, H.F., Dixon, D.J., 1994. Volcanism and archipelagic aprons in the marquesas and Hawaiian islands. Mar. Geophys. Res. 16, 385–406. https://doi.org/10.1007/BF01203974.

Galgana, G.A., Grosfils, E.B., McGovern, P.J., 2013. Radial dike formation on Venus: insights from models of uplift, flexure and magmatism. Icarus 225 (1), 538–547. https://doi.org/10.1016/j.icarus.2013.04.020.

Galgana, G.A., McGovern, P.J., Grosfils, E.B., 2011. Evolution of large Venusian volcanoes: insights from coupled models of lithospheric flexure and magma reservoir pressurization. J. Geophys. Res.: Planets 116 (E3). https://doi.org/10.1029/2010JE003654.

Ghail, R.C., Wilson, L., 2013. A pyroclastic flow deposit on Venus. Geological Society 401, 97–106. https://doi.org/10.1144/SP401.1.

Ghail, R.C., et al., 2020. The science goal of the EnVision Venus orbiter mission. Europlanet Sci/ Congress. https://doi.org/10.5194/epsc2020-599. EPSC2020-599, 2020.

Gilmore, M.S., Head, J.W., 2018. Morphology and deformational history of tellus Regio, Venus: evidence for assembly and collision. Planet. Space Sci. 154, 5–20. https://doi.org/10.1016/j.pss.2018.02.001.

Glaze, L.S., et al., 2017. DAVINCI: deep atmosphere Venus investigation of noble Gases, chemistry, and imaging. IEEE Aerospace Conf. 1–5 https://doi.org/10.1109/AERO.2017.7943923.

Griffiths, R.W., 2000. The dynamics of lava flows. Annu. Rev. Fluid Mech. 32, 477–518. https://doi.org/10.1146/annurev.fluid.32.1.477.

Gregg, T.K.P., Fink, J.H., 2000. A laboratory investigation into the effects of slope on lava flow morphology. J. Volcanol. Geoth. Res. 96 (3–4), 145–159. https://doi.org/10.1016/S0377-0273(99)00148-1.

Grimm, R.E., Hess, P.C., 1997. The crust of Venus. In: Bougher, S.W., et al. (Eds.), Venus II: Geology, Geophysics, Atmosphere, and Solar Wind Environment. University of Arizona Press, pp. 1205–1244. https://doi.org/10.2307/j.ctv27tct5m.26.

Grosfils, E.B., Head, J.W., 1994. Emplacement of a radiating dike swarm in western Vinmara Planitia, Venus: interpretation of the regional stress field orientation and subsurface magmatic configuration. Earth Moon Planets 66, 153–171. https://doi.org/10.1007/BF00644129.

Gundmundsson, A., 1988. Formation of collapse calderas. Geology 16 (9), 808–810. https://doi.org/10.1130/0091-7613(1988)016%3C0808:FOCC%3E2.3.CO.

Gundmundsson, M.T., et al., 2016. Gradual caldera collapse at Bárdarbunga volcano, Iceland regulated by lateral magma outflow. Science 353 (6296). https://doi.org/10.1126/science.aaf8988.

Head, J.W., Coffin, M.F., 1997. Large igneous provinces: a planetary perspective. In: Mahoney, J.J., Coffin, M.F. (Eds.), American Geophysical Union, Large Igneous Provinces: Continental, Oceanic and Planetary Flood Volcanism, vol. 100. Geophysical Monograph, pp. 411–438. https://doi.org/10.1029/GM100p0411.

Head, J.W., Crumpler, L.S., Aubele, J.C., Guest, J.E., Saunders, R., 1992. Venus volcanism: classification of volcanic features and structures, associations, and global distribution from Magellan data. J. Geophys. Res.: Planets 97 (E8), 13153–13197. https://doi.org/10.1029/92JE01273.

Heiken, G., Goff, F., Stix, J., Tamanyu, S., Shafiqullah, M., Garcia, S., Hagan, R., 1986. Intracaldera volcanic activity, toledo caldera and embayment, Jemez Mountains, New Mexico. J. Geophys. Res. Solid Earth 91 (B2), 1799–1815. https://doi.org/10.1029/JB091iB02p01799.

Head, J.W., Ivanov, M.A., Basilevsky, A.T., 2024. Global geological mapping of Venus and the twenty-first-century legacy of William Smith: identification of challenges and opportunities for future research and exploration. In Geological Society, London, Special Publications 541. https://doi.org/10.1144/sp541-2023-30.

Head, J.W., Magee, K.R., Wilson, L., Pinkerton, H., 1993. Lava flow-field morphological classification and interpretation: examples from Venus. 24th Lunar and Planetary Sci. Conf. 627.

Harris, A.J.L., Rowland, S.K., 2009. Effusion rate controls on lava flow length and the role of heat loss: a review. In: Thordarsson, T., et al. (Eds.), The Geological Society, Studies in Volcanology: the Legacy of George Walker, vol. 2. Special Publications of IAVCEI, pp. 33–51. https://doi.org/10.1144/IAVCEl002.3.

Head, J.W., Wilson, L., 1992. Magma reservoirs and neutral buoyancy zones on Venus: implications for the formation and evolution of volcanic landforms. J. Geophys. Res.: Planets 97 (E3), 3877–3903. https://doi.org/10.1029/92JE00053.

Head, J.W., Wilson, L., 1986. Volcanic processes, and landforms on Venus: theory, predictions and observations. J. Geophys. Res. Solid Earth 91 (B9), 9407–9446. https://doi.org/10.1029/JB091iB09p09407.

Herrick, R.R., Dufek, J., McGovern, P.J., 2005. Evolution of large shield volcanoes on Venus. J. Geophys. Res.: Planets 110 (E1). https://doi.org/10.1029/2004JE002283.

Herrick, R.R., Hensley, S., 2023. Surface changes observed on a Venusian volcano during the Magellan mission. Science 379 (6638), 1205–1208. https://doi.org/10.1126/science.abm7735.

Ivanov, M.A., Head, J.W., 2004. Stratigraphy of small shield volcanoes on Venus: criteria for determining stratigraphic relationships and assessment of relative age and temporal abundance. J. Geophys. Res.: Planets 109 (E10). https://doi.org/10.1029/2004JE002252.

Ivanov, M.A., Head, J.W., 2011. Global geological map of Venus. Planet. Space Sci. 59 (13), 1559–1600. https://doi.org/10.1016/j.pss.2011.07.008.

Ivanov, M.A., Head, J.W., Wilson, L., 2019. Major episodes of volcanic activity at the large shield volcano Tuulikki Mons, Venus. 50th Lunar and Planetary Sci. Conf. 2132, 1272.

Jerram, D.A., Widdowson, M., 2005. The anatomy of Continental Flood Basalt Provinces: geological constraints on the processes and products of flood volcanism. Lithos 79 (3–4), 385–405. https://doi.org/10.1016/j.lithos.2004.09.009.

Jiménez-Diaz, A., Ruiz, J., Kirby, J.F., Romeo, I., Tejero, R., Capote, R., 2015. Lithospheric structure of Venus from gravity and topography. Icarus 260, 215–231.

Kargel, J.S., Komatsu, G., Baker, V.R., Strom, R.G., 1993. The volcanology of Venera and Vega landing sites and geochemistry of Venus. Icarus 103, 253–275.

Keddie, S.T., Head, J.W., 1994. Sapas Mons, Venus: evolution of a large shield volcano. Earth Moon Planets 65, 129–190. https://doi.org/10.1007/BF00644896.

Khawja, S., Ernst, R.E., Samson, C., Byrne, P.K., Ghail, R.C., MacLellan, L.M., 2020. Tesserae on Venus may preserve evidence of fluvial erosion. Nat. Commun. 11, 5789. https://doi.org/10.1038/s41467-020-19336-1.

Kiefer, W.S., Potter, E.-K., 2000. Gravity Anomalies at Venus Shield Volcanoes: Implications for Lithospheric Thickness, 31st Lunar and Planetary Science Conference, vol. 31. Abstract #1924.

Kieffer, B., Arndt, N., Lapierre, H., Bastien, F., Bosch, D., Pecher, A., Yirgu, G., Ayalew, D., Weis, D., Jerram, D.A., Keller, F., Meugniot, C., 2004. Flood and Shield Basalts from Ethiopia: Magmas from the African Superswell. J. Petrol. 45 (4), 783–834. https://doi.org/10.1093/petrology/egg112.

Lightfoot, P.C., Keays, R.R., 2005. Siderophile and chalcophile metal variations in flood basalts from the Siberian Trap, Noril'sk Region: implications for the origin of the Ni-Cu-PGE sulfide ores. Econ. Geol. 100 (3), 439–462.

Lipman, P.W., 1997. Subsidence of ash-flow calderas: relation to caldera size and magma-chamber geometry. Bull. Volcanol. 59, 198–218. https://doi.org/10.1007/s004450050186.

Lipman, P.W., 2000. Calderas. In: Sigurdsson, H. (Ed.), Encyclopedia of Volcanoes. Academic Press, pp. 643–662.

Lockwood, J.P., Lipman, P.W., 1987. Chapter 18: holocene eruptive history of Mauna Loa volcano. In: Decker, R.W., et al. (Eds.), U. S. Geological Survey Professional Paper, Volcanism in Hawaii, vol. 1350, pp. 509–535.

MacLellan, L., Ernst, R.E., El Bilali, H., Ghail, R.C., Bethell, E., 2021. Volcanic history of the Derceto large igneous province, Astkhik Planum, Venus. Earth Sci. Rev. 220, 103619 https://doi.org/10.1016/j.earscirev.2021.103619.

Magee Roberts, K., Head, J.W., 1993. Large-scale volcanism associated with coronae on Venus: implications for formation and evolution. Geophys. Res. Lett. 20 (12), 1111–1114. https://doi.org/10.1029/93GL01484.

Magee, K.P., Head, J.W., 1995. The role of rifting in the generation of melt: implications for the origin and evolution of the Lada Terra-Lavinia Planitia region of Venus. J. Geophys. Res.: Planets 100 (E1), 1527–1552. https://doi.org/10.1029/94JE02334.

McGovern, P.J., Galgana, G.A., Verner, K.R., Herrick, R.R., 2014. New constraints on volcano-tectonic evolution of large volcanic edifices on Venus from stereo topography-derived strain estimates. Geology 42 (1), 59–62. https://doi.org/10.1130/G34919.1.

McGovern, P.J., Grosfils, E.B., Galgana, G.A., Morgan, J.K., Rumpf, M.E., Smith, J.R., Zimbelman, J.R., 2015. Lithospheric flexure and volcano basal boundary conditions: keys to the structural evolution of large volcanic edifices on the terrestrial planets. Geolog. Society, London, Spl. Pub. 401 (1), 219–237. https://doi.org/10.1144/SP401.7.

McGovern, P.J., Rumpf, M.E., Zimbelman, J.R., 2013. The influence of lithospheric flexure on magm ascent at large volcanoes on Venus. J. Geophys. Res.: Planets 118 (11), 2423–2437. https://doi.org/10.1002/2013JE004455.

McGovern, P.J., Solomon, S.C., 1997. Filling of flexural moats around large volcanoes on Venus: implications for volcano structure and global magmatic flux. J. Geophys. Res.: Planets 102 (E7), 16303–16318. https://doi.org/10.1029/97JE01318.

McGovern, P.J., Solomon, S.C., 1998. Growth of large volcanoes on Venus: mechanical models and implications for structural evolution. J. Geophys. Res.: Planets 103 (E5), 11071–11101. https://doi.org/10.1029/98JE01046.

Moore, I.A.N., Kokelaar, P., 1997. Tectonic influences on piecemeal caldera collapse at Glencoe Volcano, Scotland. J. Geol. Soc. 154 (5), 765–768. https://doi.org/10.1144/gsjgs.154.5.0765.

Mouginis-Mark, P.J., 2016. Geomorphology and volcanology of Maat Mons, Venus. Icarus 277, 433–441. https://doi.org/10.1016/j.icarus.2016.05.022.

Mouginis-Mark, P.J., Robinson, M.S., 1992. Evolution of Olympus Mons caldera, Mars. Bull. Volcanol. 54, 347–360. https://doi.org/10.1007/BF00312318.

Neal, C.A., et al., 2018. The 2018 rift eruption and summit collapse of Kilauea Volcano. Science 363 (6425), 367–374. https://doi.org/10.1126/science.aav7046.

Parfitt, E.A., Head, J.W., 1993. Buffered and unbuffered dike emplacement on Earth and Venus: implications for magma reservoir size, depth, and rate of magma replenishment. Earth Moon Planets 61, 249–281.

Patrick, M.R., Orr, T.R., Swanson, D.A., Elias, T., Shiro, B., 2018. Lava Lake Activity at the Summit of Kilauea Volcano in 2016. U. S. Geological Survey Scientific Investigations, p. 58. https://doi.org/10.3133/sir20185008. *Report 2018-5008*.

Phillips, R.J., Hansen, V.L., 1994. Tectonic and magmatic evolution of Venus. Annu. Rev. Earth Planet Sci. 22, 597–656. https://doi.org/10.1146/annurev.ea.22.050194.003121.

Pinkerton, H., Norton, G., 1995. Rheological properties of basaltic lavas at sub-liquidus temperatures: laboratory and field measurements on lavas from Mount Etna. J. Volcanol. Geoth. Res. 68 (4), 307–323.

Reidel, S.P., Hooper, P.R., 1989. Volcanism and tectonism in the Columbia River flood-basalt province. In: GSA Special Papers, vol. 239. Geological Society of America. https://doi.org/10.1130/SPE239.

Roche, O., Druitt, T.H., Merle, O., 2000. Experimental study of caldera formation. J. Geophys. Res. 105, 395–416. https://doi.org/10.1029/1999JB900298. Nº B1.

Rooney, T.O., 2017. The Cenozoic magmatism of East-Africa: Part I — flood basalts and pulsed magmatism. Lithos 286–287, 264–301. https://doi.org/10.1016/j.lithos.2017.05.014.

Shellnutt, J.G., 2013. Petrological modelling of basaltic rocks from Venus: A case for the presence of silicic rocks. J. Geophys. Res.: Planets 118 (6), 1350–1364. https://doi.org/10.1002/jgre.20094.

Shimolina, A.S., Ernst, R.E., El Bilali, H., 2023. Lava Flows of Theia Mons Volcano, Beta Regio Plume Centre, Venus, 54th Lunar and Planetary Science Conference. Abstract #1159.

Simkin, T., Howard, K.A., 1970. Caldera collapse in the Galapagos Islands, 1968: The largest known collapse since 1912 followed a flank eruption and explosive volcanism within the caldera. Science 169 (3944), 429–437. https://doi.org/10.1126/science.169.3944.429.

Smrekar, S., et al., 2022. VERITAS (Venus Emissivity, radio science, InSAR, topography, and spectroscopy): a Discovery mission. IEEE Aerospace Conf. (AERO) 1–20. https://doi.org/10.1109/AERO53065.2022.9843269.

Solomatov, V., Moresi, L., 1996. Stagnant lid convection on Venus. J. Geophys. Res.: Planets 101 (E2), 4737–4753. https://doi.org/10.1029/95JE03361.

Solomon, S.C., Smrekar, S.S., Bindschandler, D.L., Grimm, R.E., Kaula, W.M., McGill, G. E., Phillips, R.J., Saunders, R.S., Schubert, G., Squyres, S.W., Stofan, E.R., 1992. Venus tectonics: an overview of Magellan observations. J. Geophys. Res.: Planets 97 (E8), 13199–13255. https://doi.org/10.1029/92JE01418.

Stern, R.J., Gerya, T., Tackley, P.J., 2018. Stagnant lid tectonics: perspectives from silicate planets, dwarf planets, large moons, and large asteroids. Geosci. Front. 9 (1), 103–119. https://doi.org/10.1016/j.gsf.2017.06.004.

Stofan, E.R., Guest, J.E., Copp, D.L., 2001. Development of large volcanoes on Venus: constraints from Sif, Gula, and Kunapipi Montes. Icarus 152 (1), 75–95. https://doi.org/10.1006/icar.2001.6633.

Sundararajan, V., 2021. Tradespace Exploration of Space System Architecture and Design for India's Shukrayaan-1, Venus Orbiter Mission. American Institute of Aeronautics and Astronautics, ASCEND 2021 Forum.

Tanaka, K.L., 1994. The Venus Geologic Mappers' Handbook, second ed. U. S. Department of the Interior, and the U. S. Geological Survey, USGS open-file report, pp. 94–438.

Trasatti, E., Acocella, V., Di Vito, M.A., Del Gaudio, C., Weber, G., Aquino, I., Caliro, S., Chiodini, G., de Vita, S., Ricco, C., Caricchi, L., 2019. Magma magma Degassing as a source of long-Term Seismicity at volcanoes: the Ischia island (Italy) case. Geophys. Res. Lett. 46 (24), 14421–14429. https://doi.org/10.1029/2019GL085371.

Varga, R. J., B. M. Smith, Evolution of the Early Oligocene Bonanza Caldera, northeast San Juan Volcanic Field, Colorado, J. Geophys. Res. Solid Earth, Vol. 89, Issue B10,1984 8679-8694. https://doi.org/10.1029/JB089iB10p08679..

Wadge, G., Lopes, R.M.C., 1991. The lobes of lava flows on Earth and Olympus Mons, Mars. Bull. Volcanol. 54, 10–24. https://doi.org/10.1007/BF00278203.

Walker, G.P.L., 1971. Compound and simple lava flows and flood basalts. Bull. Volcanol. 35 (Nº 3), 579–590. https://doi.org/10.1007/BF02596829.

Walker, G.P.L., 1973. Lengths of lava flows. Phil. Trans. Roy. Soc. Lond. Math. Phys. Sci. 274, 107–118.

Wang, C., T. Song, P. Shi, M. Li, Q. Fan, China's Space Science Program (2025–2030): Strategic Priority Program on Space Science (III), Chin. J. Space Sci., Vol. 42, Issue 4, 514–518. https://doi.org/10.11728/cjss2022.04.yg01..

Watts, A.B., ten Brink, U.S., 1989. Crustal structure, flexure, and subsidence history of the Hawaiian Islands. J. Geophys. Res. Solid Earth 94 (B8), 10473–10500. https://doi.org/10.1029/JB094iB08p10473.

Way, M.J., Del Genio, A.D., Kiang, N.Y., Sohl, L.E., Grinspoon, D.H., Aleinov, I., Kelley, M., Clune, T., 2016. Was Venus the first habitable world of our solar system? Geophys. Res. Lett. 43 (16), 8376–8383. https://doi.org/10.1002/2016GL069790.

Way, M.J., Ernst, R.E., Scargle, J.D., 2022. Large scale volcanism and the heat-death of terrestrial worlds. Planet. Sci. J. 3 https://doi.org/10.3847/PSJ/ac6033. Nº 4.

Wilhelms, D.E., 1990. Geologic mapping. In: Greeley, R., Batson, R.M. (Eds.), Planetary Mapping. Cambridge University Press, pp. 208–260.

Wilson, L., Head III, J.W., 1983. A comparison of volcanic eruption processes on Earth, Moon, Mars, Io and Venus. Nature 302, 663–669. https://doi.org/10.1038/302663a0.

Wilson, L., Head, J.W., 2002. Tharsis-radial graben systems as the surface manifestation of plume-related dike intrusion complexes: models and implications. J. Geophys. Res.: Planets 107 (E8), 1-1–1-24. https://doi.org/10.1029/2001JE001593.

Yamada, I., 2016. Thiessen polygons. In: International Encyclopedia of Geography: People, the Earth, Environment and Technology. https://doi.org/10.1002/9781118786352.wbieg0157.

Zasova, L.V., Gorinov, D.A., Eismont, N.A., Kovalenko, I.D., Abbakumov, A.S., Bober, S. A., 2019. Venera-D: a design of an automatic space station for Venus exploration. Sol. Syst. Res. 53, 506–510. https://doi.org/10.1134/S0038094619070244.